Biophysical *Journal*
Article

Biophysical Society

Partitioning and Enhanced Self-Assembly of Actin in Polypeptide Coacervates

Patrick M. McCall,[1,2] Samanvaya Srivastava,[3,7] Sarah L. Perry,[3] David R. Kovar,[4,5] Margaret L. Gardel,[1,2,6,*] and Matthew V. Tirrell[3,7,*]

[1]Department of Physics, [2]James Franck Institute, [3]Institute for Molecular Engineering, [4]Department of Molecular Genetics and Cell Biology, [5]Department of Biochemistry and Molecular Biology, and [6]Institute for Biophysical Dynamics, The University of Chicago, Chicago, Illinois; and [7]Argonne National Laboratory, Argonne, Illinois

ABSTRACT Biomolecules exist and function in cellular microenvironments that control their spatial organization, local concentration, and biochemical reactivity. Due to the complexity of native cytoplasm, the development of artificial bioreactors and cellular mimics to compartmentalize, concentrate, and control the local physico-chemical properties is of great interest. Here, we employ self-assembling polypeptide coacervates to explore the partitioning of the ubiquitous cytoskeletal protein actin into liquid polymer-rich droplets. We find that actin spontaneously partitions into coacervate droplets and is enriched by up to ~30-fold. Actin polymerizes into micrometer-long filaments and, in contrast to the globular protein BSA, these filaments localize predominately to the droplet periphery. We observe up to a 50-fold enhancement in the actin filament assembly rate inside coacervate droplets, consistent with the enrichment of actin within the coacervate phase. Together these results suggest that coacervates can serve as a versatile platform in which to localize and enrich biomolecules to study their reactivity in physiological environments.

INTRODUCTION

The biological functions of intracellular organelles are defined by the composition and properties of the compartments, which often differ significantly from that of bulk cytoplasm. Well-known examples include the acidic pH of lysosomes and the mitochondrial redox potential (1). Although the compartmentalization of these organelles requires a lipid bilayer as a physical barrier, recent work has shown that organelles can also form as phase-separated droplets that do not require such a membrane (2,3). The physicochemical properties of membraneless organelles likely regulate partitioning and reactivity of biomolecules, thereby serving an important role in their physiological function. The compositional complexity of individual cellular bodies, granules, and organelles poses a major challenge in discerning general mechanisms for partitioning and reaction regulation. One useful strategy has been to reduce compositional complexity by in vitro reconstitution of cellular bodies (4,5). However, the sequence and structural complexity of natural biopolymers make systematic variation of microenvironment properties difficult.

A complementary approach is to selectively tune the physical and chemical properties of phase-separated microenvironments through the rational design of synthetic polymers that spontaneously phase-separate via known mechanisms, and then use these materials as a platform to study biomolecule partitioning and reactivity. For instance, charged homopolymers (polyelectrolytes) form polymer-dense liquid phases via complex coacervation (6,7) and localize charged proteins (8–11) and small molecules (12,13). Precise chemical control of polypeptide-based polyelectrolytes allows for fine-tuning of several physiochemical properties of the coacervate phase (7,14), including functional groups, water content, viscosity, and surface tension, thereby enabling systematic investigations of protein interactions and activities in controlled microenvironments (15,16). Knowledge of the general mechanisms by which microenvironment properties tune protein partitioning and activity could provide needed insight into the

Submitted June 22, 2017, and accepted for publication February 20, 2018.

*Correspondence: gardel@uchicago.edu or mtirrell@uchicago.edu

Patrick M. McCall and Samanvaya Srivastava contributed equally to this work.

Margaret L. Gardel and Matthew V. Tirrell contributed equally to this work.

Patrick M. McCall's present address is Max Planck Institute of Molecular Cell Biology and Genetics, Dresden, Germany.

Samanvaya Srivastava's present address is Department of Chemical and Biomolecular Engineering, University of California, Los Angeles, Los Angeles, California.

Sarah L. Perry's present address is Department of Chemical Engineering, University of Massachusetts Amherst, Amherst, Massachusetts.

Editor: Enrique De La Cruz.

https://doi.org/10.1016/j.bpj.2018.02.020

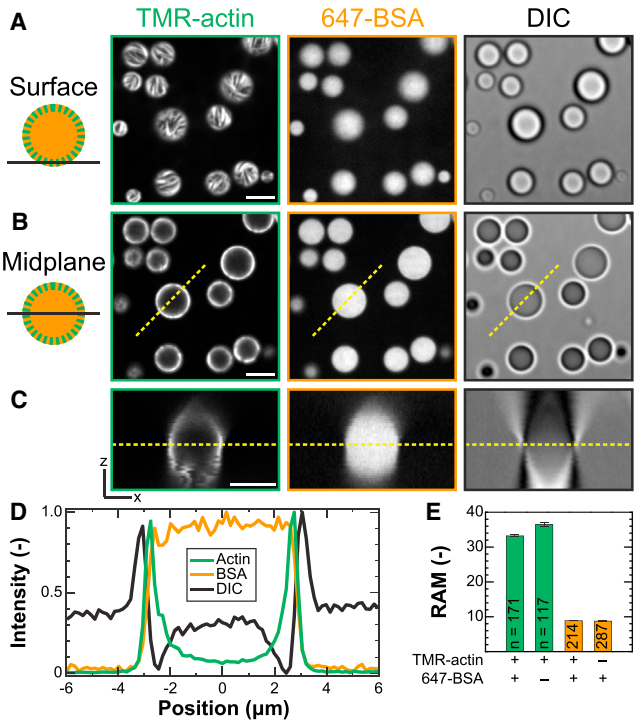

FIGURE 1 F-actin localizes to the periphery of polypeptide coacervates. (*A* and *B*) Confocal fluorescence (*left* and *middle*) and DIC (*right*) micrographs are shown of polypeptide coacervates containing both TMR-actin (*green*) and 647-BSA (*orange*) on nonadherent substrates. (*A* and *B*) Focal plane is at the interface of the coacervates and the substrate (surface (*A*)), or near the midplane of the largest droplet (*B*), indicated by the dashed yellow line in (*C*). (*C*) An *x*-*z* cross section is formed from the intensity values along the dashed lines in (*B*) evaluated in all planes of a confocal z-stack. Scale bar, 5 μm in (*A*–*C*). (*D*) Normalized intensity line scans are given along the dashed yellow lines as indicated in (*B*) and (*C*). (*E*) Average RAM is given for coacervates in samples containing 0.5 μM actin alone, 0.5 μM BSA alone, or 0.25 μM actin and 0.25 μM BSA together (*A*–*D*). Error bars denote standard error of the mean. The number of droplets included in each condition is listed on the bar. Conditions are 0.5 μM total protein (0.25 μM Mg-ATP-actin (47% TMR-labeled) and 0.25 μM BSA (91% Alexa-647-labeled)) incubated with 5 mM pLK before addition of 5 mM pRE in 50 mM KCl, 1 mM $MgCl_2$, 1 mM EGTA, 10 mM imidazole (pH 7.0), and 72 μM ATP (all concentrations final). To see this figure in color, go online.

function of membraneless organelles as well as design principles for synthetic biology and engineering applications.

Here, we report the spontaneous partitioning and polymerization of the cytoskeletal protein actin inside model polypeptide coacervates (17,18) as a proof-of-concept demonstration of coacervates as bioreactors for studying biomolecular reactions in cell-like physical environments. Our results establish polyelectrolyte complex coacervates as a viable platform to study mechanisms of partitioning and biochemical regulation by controlled perturbation of a condensed-phase microenvironment.

MATERIALS AND METHODS

Solutions containing pLK/pRE coacervates and fluorescently labeled proteins were imaged on a spinning disk confocal microscope. We quantify the partitioning of the proteins BSA and actin to pLK/pRE coacervates by measuring the relative accumulated mass (RAM) of protein localized to coacervates. RAM values are calculated from thresholded fluorescence images acquired near droplet midplanes ~20 min after the final mixing reaction. With the exception of Fig. 4, the RAM values reported represent the average fluorescence intensity within thresholded droplets normalized by the average fluorescence intensity exterior to droplets, and thus include contributions from both the droplet interior and periphery. For the analysis in Fig. 4, thresholded droplets were further subdivided into interior and peripheral regions, and auxiliary RAM values for each of these regions are reported.

The RAM is related to a more commonly used quantity known as the equilibrium partition coefficient, which is defined as the ratio of the concentration of the molecule inside the partitioning medium to that of the molecule outside the partitioning medium (4). At equilibrium, the RAM of a molecule in a partitioning medium is equal to its partition coefficient in that medium. The RAM values reported for BSA are thus equivalent to equilibrium partition coefficients.

In contrast, interpretation of the RAM of actin in coacervates measured by fluorescence in terms of equilibrium partition coefficients is fundamentally more challenging for two reasons. First, because actin filaments of different lengths are distinct chemical species, each with their own chemical potential, a partition coefficient for all species of actin together is ill-defined. Rather, a separate partition coefficient is required for each polymer species present (19). Second, the average TMR-fluorescence value we measure is insensitive to the distribution of actin filament lengths present, and thus the individual concentrations of each species present are unknown. Instead, the average TMR-fluorescence is directly proportional to the total mass of actin monomers present. For these reasons, we report the mass of actin accumulated in the coacervate, relative to that in solution outside of coacervates, instead of a partition coefficient. We expect that these two challenges are not specific to actin, but rather would hold for any instance in which partitioning is linked to a reaction in which the reactants and products cannot be readily distinguished and are therefore all included in the accumulated mass.

An additional practical complication is that the timescales for the equilibration of both the reaction and reactant partitioning can be quite long, particularly for equilibration of the actin filament length distribution by diffusive length fluctuations (20). Additional details of all experimental methods and analysis can be found in the Supporting Material.

RESULTS

We use a model coacervate system (18) composed of the polycation poly-L-lysine (pLK) and the polyanion poly-(L,D)-glutamic acid (pRE), typically with ~100 amino acids per polypeptide (Table S1). Phase separation at room temperature is rapid; initially clear aqueous solutions become visibly turbid in seconds upon mixing of pLK- and pRE-containing solutions at total polypeptide concentrations of 10 μM or more (Movie S1), and this is driven primarily by the release of condensed counterions (21). The presence of a polydisperse size distribution of polypeptide-rich coacervate droplets in solution, ranging in size from $\sim 0.4 < R < 4$ μm, is confirmed directly by differential interference contrast (DIC) microscopy (Fig. 1, *A*–*C*; Movie S1). The round, droplet-like appearance of the condensed pLK/pRE coacervate phase is suggestive of a fluid phase (18). Under similar conditions, the surface tension has been measured to be $\gamma \sim 1$ mN/m (22). Consistent with liquid-like properties on the timescale of seconds and longer, merging pLK/pRE droplets rapidly coalescence

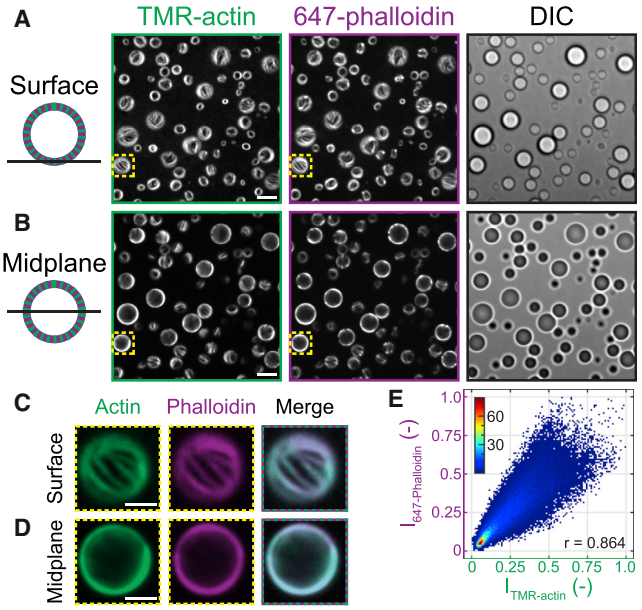

FIGURE 2 Linear actin filaments maintain canonical F-actin structure. (*A* and *B*) Confocal fluorescence (*left* and *middle*) and DIC (*right*) micrographs are given of polypeptide coacervates containing TMR-actin (*green*) after the addition of Alexa-647-Phalloidin (*purple*) on nonadherent substrates. (*A* and *B*) Focal plane is at the interface of the coacervates and the substrate (surface (*A*)) or near the midplane of the largest droplet in the field of view (*B*). Scale bars, 5 μm. Conditions are 0.5 μM Mg-ATP-actin (47% TMR-labeled) incubated with 5 mM pLK before addition of 5 mM pRE in 50 mM KCl, 1 mM $MgCl_2$, 1 mM EGTA, 10 mM imidazole (pH 7.0), and 72 μM ATP (all concentrations final). 0.25 μM Alexa-647-Phalloidin was flown into the chamber in the same buffer after droplets had sedimented. (*C* and *D*) False-colored fluorescence images are given of the regions outlined in yellow boxes in (*A*) and (*B*) from the surface (*C*) and midplane (*D*). Right column shows a merge. Scale bars, 2 μm. (*E*) Correlation between normalized TMR-actin and 647-phalloidin fluorescence intensity values is shown for all coacervate-positive pixels in (*A*). Colors represent count density. Pearson's correlation coefficient is $r = 0.864$. To see this figure in color, go online.

into a single, larger droplet (Fig. S1). From coalescence observations, we estimate the inverse capillary velocity $v^{-1} = \eta/\gamma = 1.6$ ms/μm (Fig. S1 (5,23)). This yields a viscosity of $\eta = 1.6$ Pa·s, ~1000-fold higher than water. Thus, this simple model system is sufficient to create viscous phase-separated droplets with picoliter volumes.

Charged proteins spontaneously partition into coacervate droplets

Using a previously published protocol, proteins are mixed with the cationic pLK before initiation of phase separation by the addition of anionic pRE (8). It was previously found that the negatively charged protein BSA localizes preferentially to pLK/pRE coacervates, and is uniformly distributed within them (Fig. 1, *A–D*; Fig. S2). This preference for the coacervate phase is described quantitatively by a partition coefficient, defined here as the ratio of fluorescence intensity inside to outside the coacervates. We find an average partition coefficient of $PC_{avg} \cong 8$, regardless of whether BSA is added to solution before or after phase separation (Fig. 1 *E*; Fig. S3), which is indicative of spontaneous partitioning.

Here, we study the partitioning of actin, a cytoskeletal protein that self-assembles to form linear filaments (F-actin). Actin monomers and the chemically inert BSA are globular proteins of similar size (42 and 66 kDa, respectively) and carry comparable negative charge (isoelectric points of 5.23 and 5.60) (24). We find that actin also partitions to pLK/pRE coacervates and immediately observe linear structures localized preferentially to the coacervate periphery (Fig. 1, *A–D*).

Due to the polymerization of actin into filaments, which results in a monomer-polymer equilibrium of actin within the coacervate that is coupled to the exterior monomer pool, interpretation of these intensities as an equilibrium partition coefficient is difficult (see Materials and Methods). However, by integrating the total actin intensity localized to a droplet at a given timepoint after reaction initiation, we can calculate the RAM at that time. In the case of equilibrium partitioning of an inert molecule, such as BSA, the RAM measured at equilibrium is equivalent to the partition coefficient. This equivalence no longer holds when partitioning is linked to a reaction in which the reactants and products are both included in the accumulated mass, as is the case for actin monomer and filaments; rather, the RAM of actin reflects the partitioning of actin monomer and filament species of all lengths, which may or may not be equilibrated at the time of measurement. We find that the RAM of actin 20 min after assembly initiation is fourfold higher than that for BSA (Fig. 1 *E*). Interestingly, the RAM of BSA and actin are the same whether one or both proteins are present in solution (Fig. 1 *E*; Fig. S2). This suggests that, under the conditions explored here, BSA and actin do not compete directly for space in the coacervate. Both partitioning and peripheral localization of actin are robust to the order of addition (Fig. S4).

Self-assembled F-actin of canonical structure localizes to the coacervate periphery

To test whether the linear actin structures are bona fide F-actin, we stained with fluorescently labeled phalloidin (647-phalloidin). Phalloidin is a small, uncharged toxin recognized for its ability to specifically bind to F-actin (25). 647-phalloidin was introduced into the solution after the coacervate formation and actin assembly, and found to localize along the linear actin structures. Confocal fluorescence micrographs at both the coverslip surface (Fig. 2, *A* and *C*) and droplet midplane (Fig. 2, *B* and *D*) reveal strong colocalization of phalloidin fluorescence to the linear actin structures with a Pearson's correlation coefficient of 0.86 (Fig. 2 *E*; Supporting Material). This provides strong evidence that these linear actin-rich structures are

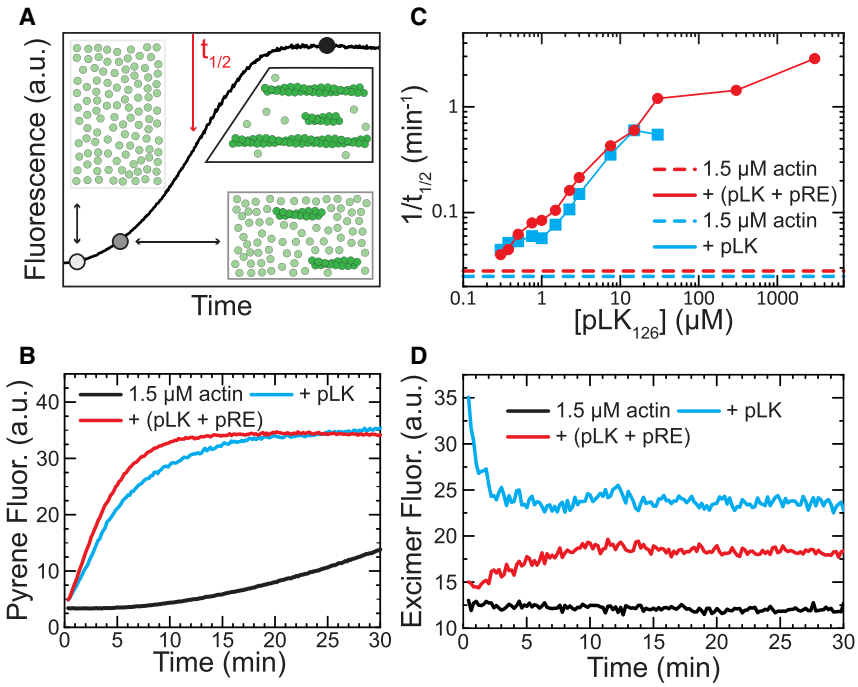

FIGURE 3 Coacervates and poly-L-lysine enhance actin assembly via different mechanisms. (*A*) Cartoon depicts the time course for spontaneous actin assembly monitored by changes in pyrene-actin fluorescence. (*B*) Spontaneous assembly is shown of 1.5 μM Mg-ATP-actin (12% pyrene-labeled) alone (*black*), with 3 μM pLK (*cyan*), or with 3 μM pLK and 3 μM pRE (*red*). (*C*) The assembly rate ($1/t_{1/2}$) is shown for 1.5 μM actin samples with pLK alone (*cyan*) or equal concentrations of pLK and pRE (*red*) as a function of the concentration of pLK. Dashed lines denote the assembly rate of 1.5 μM actin alone measured in parallel with pLK-containing (*cyan dashed*) or pLK- and pRE-containing (*red dashed*) samples. (*D*) Timecourse of pyrene excimer fluorescence during spontaneous assembly is given of 1.5 μM Mg-ATP-actin (12% pyrene-labeled) alone (*black*), with 3 μM pLK alone (*cyan*), or with 3 μM pLK and 3 μM pRE together (*red*). In all experiments with polypeptides, Mg-ATP-actin is incubated with variable pLK in low salt before addition of pRE (*red*) or a buffer blank (*cyan*) in 50 mM KCl, 1 mM $MgCl_2$, 1 mM EGTA, 10 mM imidazole (pH 7.0), and 72–150 μM ATP (all concentrations final). To see this figure in color, go online.

composed of F-actin of canonical structure. Given the brightness of the F-actin structures, and previous work demonstrating that concentrations of polycations (and pLK in particular) lower than those in the coacervate phase are sufficient to bundle F-actin (26), we presume that the structures visible in Figs. 1 and 2 are F-actin bundles, rather than individual filaments.

Actin assembly is enhanced in coacervates

Having demonstrated that actin polymerization proceeds in pLK/pRE coacervates, we next ask to what extent the coacervate microenvironment impacts the reaction rate. Actin is a convenient model protein for this purpose, owing to the existence of established spectroscopic tools for quantitatively monitoring assembly kinetics (27). In particular, the fluorescence intensity of the pyrene fluorophore increases ~20-fold when pyrene-labeled monomers are incorporated into filaments and is a well-established method to track actin assembly (27), as depicted in the schematic in Fig. 3 *A*. In solution, the polymerization time course of 1.5 μM actin shows a characteristic lag phase, indicative of the kinetically slow filament nucleation step (28), followed by a phase of rapid growth and then saturation once a steady state is reached (Fig. 3 *A*) (27). At this actin concentration, the initial lag phase is typically ~10 min and steady state is reached in ~120 min (Fig. 3 *B*, *black*). The presence of pLK/pRE coacervates eliminates the lag phase and steady state is achieved within 10 min (Fig. 3 *B*, *red*). Thus, actin filament assembly is stimulated significantly by pLK/pRE coacervates.

To assess reaction kinetics quantitatively, we estimate the assembly rate $1/t_{1/2}$, defined as the inverse of the time at which the pyrene fluorescence intensity reaches half of its relative change during the course of actin polymerization (Fig. 3 *A*; Supporting Material). The actin assembly rate $1/t_{1/2}$ increases from 0.03 to >1 min^{-1} as the total pLK concentration increases from 0.3 to 30 μM, while maintaining a pLK/pRE ratio of 1 (Fig. 3 *C*). Above 30 μM, the assembly rate saturates. Thus, the actin assembly rate is enhanced by nearly two orders of magnitude in the presence of coacervates (Figs. 1, 2, and 4).

Polylysine and coacervates stimulate actin assembly via distinct mechanisms

One possible explanation for the enhanced assembly rate is polycation-mediated F-actin nucleation. Polylysine has been shown to promote formation of antiparallel actin dimers (29) that nucleate F-actin (30,31). Spontaneous assembly of pyrene-labeled actin in the presence of pLK shows a concentration-dependent increase in the rate of actin assembly (Fig. 3, *B* and *C*, *blue data*). It is tempting to compare the filament formation rate in solution directly to the rates observed within coacervates. However, the local pLK concentration within the coacervate phase is actually much higher, on the order of 1–3 M (see Supporting Material), such that the pLK concentrations reported in Fig. 3 *C* should not be directly compared. Furthermore, pLK/pRE interactions within the coacervate could limit pLK-mediated antiparallel dimer formation.

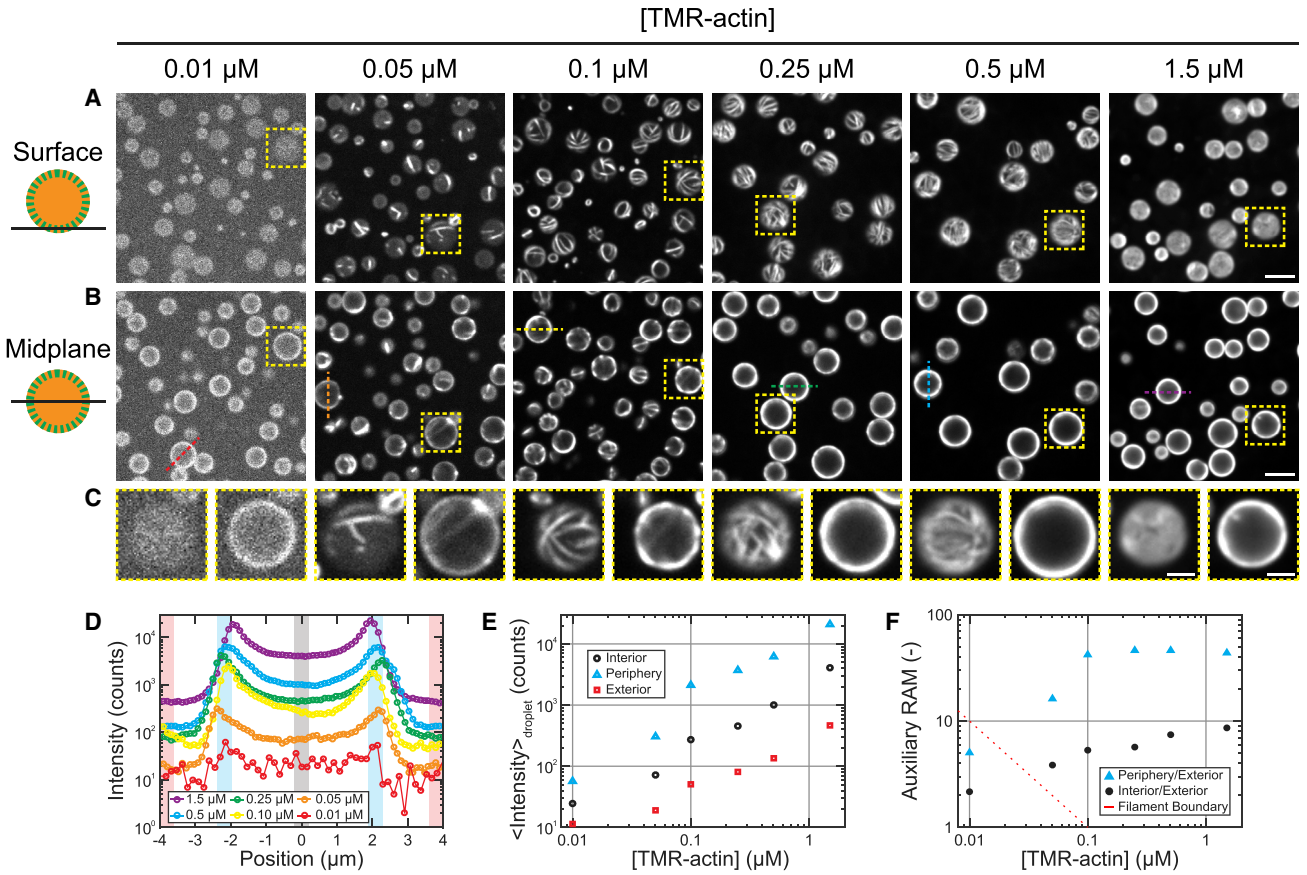

FIGURE 4 Partitioning increases the local protein concentration in coacervates. (*A* and *B*) Confocal fluorescence micrographs are given of polypeptide coacervates containing variable concentrations of TMR-actin on nonadherent substrates, focused at the interface of the coacervates and the substrate (surface, *A*), or near the droplet midplane (*B*). Contrast is adjusted individually for each concentration of TMR-actin, but is consistent between confocal slices for each condition. (*C*) Magnified images are given of the yellow boxed regions outlined in (*A*) and (*B*). Scale bars, 5 μm (*A* and *B*) and 2 μm (*C*). (*D*) Fluorescence intensity is given along the colored dashed lines in (*B*). (*E*) Mean fluorescence intensity is given of interior (*circle*, *black*), periphery (*triangle*, *cyan*), and exterior (*square*, *red*) of coacervates droplets, obtained from the black-, cyan-, and red-shaded regions in (*D*). (*F*) Auxiliary RAM values, showing ratios of peripheral to exterior fluorescence (*triangles*, *cyan*) and interior to exterior fluorescence (*circles*, *black*), are given for the data in (*D*) and (*E*). Red line indicates where product of the auxiliary RAM value and the total actin concentration equals the critical concentration for actin assembly of ~0.1 μM. Filaments are expected to the right of the red line, but not to the left. Conditions are 47% TMR-labeled Mg-ATP-actin at a range of concentrations, incubated with 5 mM pLK either alone (1.5- and 0.5-μM actin) or with 0.25 μM 91% Alexa-647-labeled BSA (0.25-, 0.1-, 0.05-, 0.01-μM actin) before addition of 5 mM pRE in 50 mM KCl, 1 mM $MgCl_2$, 1 mM EGTA, 10 mM imidazole (pH 7.0), and 72 μM ATP (all concentrations final). To see this figure in color, go online.

To test whether pLK-stabilized antiparallel actin dimers contribute to the assembly of F-actin in pLK/pRE coacervates, we monitored pyrene excimer fluorescence (29). In the absence of pLK, 1.5 μM actin displays no change in pyrene excimer fluorescence during the nucleation-dominated early phase of assembly (Fig. 3 *D*, *black*). In the presence of pLK, excimer fluorescence is highest during the initial nucleation phase, and decays rapidly as assembly proceeds (Fig. 3 *D*, *blue*). This excimer fluorescence time course is the hallmark of actin assembly mediated by pLK-stabilized antiparallel actin dimers (29). Importantly, in the presence of pLK/pRE coacervates, excimer fluorescence does not have these features characteristic of antiparallel dimer-mediated nucleation events (Fig. 3 *D*, *red*). These data strongly suggest that pLK-mediated nucleation is not the dominant mechanism by which actin assembly is enhanced in pLK/pRE coacervates.

Partitioning increases the local protein concentration in coacervates

A direct consequence of partitioning is that the local actin concentration in the coacervate phase is higher than that in the polymer-dilute phase. Thus, an alternate mechanism underlying enhanced assembly rates is an increased local actin concentration, c_{local}, within coacervates.

We tested this possibility by varying the global actin concentration, c_{global}, from 0.01 to 1.5 μM. The threshold monomer concentration, or critical concentration c^*, required for polymerization of Mg-ATP-actin, is ~0.1 μM (32,33). If

actin is concentrated in coacervate droplets ~30-fold via partitioning, we would expect actin assembly within coacervates at global actin concentrations of ~0.003 μM. Importantly, we observe coacervate-associated F-actin at global actin concentrations as low as 0.05 μM (Fig. 4, *A–C*). Interestingly, we observe peripherally biased partitioning of actin to pLK/pRE coacervates at all actin concentrations examined, even at the lowest concentration (0.01 μM) for which no filaments are clearly discernible. We note that the density of peripherally localized F-actin changes as a function of the global actin concentration. Whereas isolated filaments or bundles are visible at 0.05 μM, an F-actin shell too dense to resolve individual structures forms at 1.5 μM (Fig. 4, *A–C*).

To systematically characterize the localization of actin fluorescence, we examined fluorescence intensity line scans through the midplane, depicted in Fig. 4 *B* and shown in Fig. 4 *D*. These curves may be divided into three regions: the droplet exterior (*red*), periphery (*blue*), and interior (*black*). Under each experimental condition, fluorescence is highest at the droplet periphery, followed by the droplet interior. The lowest fluorescence intensities are consistently observed exterior to droplets (Fig. 4 *E*). The fluorescence increases nearly linearly with actin concentration both inside and outside the coacervate droplets (Fig. 4 *E*).

In addition to the average RAM of actin, we report two auxiliary RAM values derived from these intensity profiles: one for the ratio of droplet periphery (maximum observed intensity) to average intensity in the exterior of the droplet (RAM_{Periph}) (Fig. 4 *F*, *blue*/*red*), and a second for the ratio of droplet interior intensity (near the center of the droplet) to the average intensity in the exterior (RAM_{Int}) (Fig. 4 *F*, *black*/*red*). Both of these auxiliary RAM values are greater than unity, indicative of partitioning of actin to the polymer-dense coacervate phase from the polymer-dilute phase. RAM_{Periph} and RAM_{Int} both tend to reach plateaus for actin concentrations >0.1 μM; RAM_{Periph} values grow almost 10-fold before stabilizing at ~45 once the global actin concentration reaches 0.1 μM, whereas RAM_{Int} values increase over the range of actin concentrations investigated in this study, and appear to approach a plateau value of ~10. The saturation of the RAM_{Periph} with global actin concentration suggests that exchange of protein between the polymer-dense and -dilute phases occurs readily, as has been reported in other liquid phase-separated systems (4).

DISCUSSION

We present proof-of-concept experiments demonstrating that a polypeptide-based complex coacervate can be used as a model bioreactor to control the localization and activity of the self-assembling cytoskeletal protein actin. We find that actin partitions spontaneously to the coacervate phase, and that its partitioning is not influenced by BSA. Strong partitioning of actin to pLK/pRE coacervates increases the local actin concentration, contributing substantially to a >50-fold increase in the actin assembly rate at the highest concentrations of actin and coacervate. Actin filaments of canonical structure localize preferentially to the coacervate periphery, effectively forming core-shell particles, with the actin shell density controlled by the actin concentration.

Partitioning versus encapsulation of client proteins

Previous work interpreted the preferential localization of the client protein to coacervate phases as "encapsulation" (8,34,35). The implication of this language is that exchange of client molecules between the coacervate and dilute phases is either nonexistent or so small as to be negligible, as with encapsulation within lipid vesicles or emulsion droplets (36,37). Indeed, Black et al. (8) argued that entry of the large (66 kDa) client BSA into pLK/pRE coacervates requires the formation of an intermediate electrostatic complex between the client and an oppositely charged polyelectrolyte in solution before phase separation, and that client release is triggered by pH-induced dissolution of the coacervate phase (8).

Our present results are more consistent with a molecular view termed "partitioning" (4), where the partition coefficient reflects the equilibration of steady fluxes of client molecules into and out of the coacervate phase. For instance, we observe partitioning of BSA and actin within ~30 s upon addition of either to preformed pLK/pRE coacervates (Fig. S3). Given the very low polypeptide concentration in the dilute phase (<30 nM pLK), this suggests that recruitment of the client to the coacervate does not require the formation of an intermediate complex with a polyelectrolyte. Further, the recovery of BSA fluorescence after photobleaching of an entire coacervate droplet directly demonstrates exchange of partitioned proteins with the exterior pool (Fig. S5). Although we expect pLK/pRE coacervates to retain zero net electrical charge (38), both in the presence and absence of partitioned client proteins, we anticipate that the nonzero charge on both actin and BSA plays a direct role in determining the magnitude of the RAM measured here, as has been shown for super-charged GFP-variants in another model coacervate system (39).

Equilibrium partitioning in synthetic polypeptide coacervates is reminiscent of other recent in vitro work wherein client proteins of low-valency spontaneously partition into liquid phase-separated structures composed of high-valency scaffold proteins (4), as well as in coacervates formed from natural biopolymers (39). This is particularly interesting in that binding is mediated by specific low-affinity protein-protein interactions in the former case, in contrast to the nonspecific electrostatic interactions presumed in the case of coacervates. This suggests that the capacity to selectively partition client molecules may be a general property of

condensed liquid-like phases, independent of the interactions driving partitioning. Here, the coupling of actin partitioning to polymerization within coacervates significantly delays the equilibration of either process, as monomer consumption by the polymerization reaction maintains a chemical potential difference for monomer between the dilute and condensed phases, resulting in the net partitioning of additional monomer. It will be interesting for future studies to explore how the relative timescales of client partitioning and reactions direct compositional maturation of condensed phases.

Origin of peripheral F-actin localization

Below, we examine three nonmutually exclusive physical mechanisms for the peripheral localization of F-actin in coacervates droplets: filament buckling, macromolecular depletion, and interfacial adsorption.

F-actin does not appear to protrude from micron-sized coacervate droplets, suggesting that coacervate surface tension may play a role in confining F-actin. One mechanism for peripheral filament localization is that surface tension causes filaments to buckle once the contour length exceeds the droplet diameter. A comparison of the energy required to increase the coacervate surface area to accommodate a protruding filament of length L and diameter d with a cylindrical cap, $E_{\text{Area}} = \pi d(L - 2R)\gamma$, with the energy required to bend the filament into a circular arc with radius R equal to that of the droplet, $E_{\text{Bend}} = (k_{\text{B}}Tl_p/2)\int_0^L |1/R|^2 ds = (k_{\text{B}}Tl_pL/2R^2)$, yields the shortest length greater than $2R$ for which bending is energetically favorable:

$$L^* = \frac{2R}{1 - \dfrac{k_{\text{B}}Tl_p}{2\pi d\gamma R^2}}, \tag{1}$$

where k_{B} is the Boltzmann constant, T is temperature, and $l_p = 10\ \mu$m is the persistence length of F-actin (40). In a 1-μm-diameter coacervate droplet with the surface tension $\gamma = 1$ mN/m (22) at room temperature, bending is preferable for filaments longer than $\sim 1\ \mu$m. Coacervate surface tension is thus sufficient to bend F-actin with contour lengths larger than the droplet diameter. However, the observation that filaments and bundles even shorter than the droplet diameter are peripherally localized (0.05 μM; Fig. 4, *A–C*) indicates that surface tension-induced buckling cannot be the sole cause.

The peripheral localization of F-actin is reminiscent of the well-known crowding of F-actin to interfaces observed in the presence of macromolecular crowding agents (41,42), which arises from depletion interactions (43). To assess this, we estimate the osmotic pressure needed to crowd F-actin to an interface to be $\Pi^* \cong 450$ Pa (Supporting Material). We estimate the osmotic pressure of the coacervate interior as that arising from a solution of flexible polymers characterized by a mesh size (44), ξ, as $\Pi = k_{\text{B}}T/\xi^3$. This suggests that a coacervate with mesh size $\xi \leq 20$ nm would generate sufficient osmotic pressure to drive peripheral localization of F-actin. We estimate the mesh size of our pLK/pRE coacervates to be 2–3 nm (Supporting Material), which supports the plausibility of a depletion-based mechanism. Noting the empirical observation that long filaments crowd more readily than short ones, macromolecular depletion could preferentially crowd long, high-aspect ratio filaments and bundles, leaving short filaments, actin monomer, and BSA uniformly distributed. A discrepancy with this model, however, is the observation that, unlike BSA, actin filaments are not mobile within the interior (Fig. S5). This, suggests that, although osmotic pressure may be sufficient for peripheral localization, the limited F-actin mobility within coacervates would preclude this from being the dominant mechanism for long filaments.

An additional, nonmutually exclusive mechanism for peripheral localization of F-actin is filament adsorption to the coacervate/bulk interface. For example, electrostatic interactions between F-actin and the coacervate could drive adsorption in a process akin to that of polyelectrolyte-mediated emulsion stabilization (45). Alternately, a difference in the interfacial tensions between F-actin and the solution and the coacervate, respectively, could drive localization of filaments to the coacervate/solution interface, such as seen in Pickering emulsions (46). In support of an adhesion-based mechanism, we note that filaments occasionally wrap around coacervate droplets when assembling in solution (Fig. S6; Movie S2), indicative of an attractive interaction between F-actin and the coacervate/solution interface. Our current experiments cannot conclude whether the protein is localized at the outside or inside surface of the coacervate, and future experiments with higher resolution are required.

Importantly, not all actin fluorescence is peripherally localized. Actin fluorescence intensity in the center of pLK/pRE coacervates is diffuse and enriched by as much as 10-fold compared to the surrounding solution (Fig. 4 *F*). Interior fluorescence increases with global actin concentration, which is inconsistent with the peripheral localization of all filaments. In that case, the interior fluorescence would correspond to solely actin monomers, which we would predict to have a constant local concentration of $c_{\text{local}} = c^* = 0.1\ \mu$M at steady state. This suggests that the coacervate interior contains a mixture of monomers and filaments. Given that a 250-nm filament ($\sim$90 actin subunits) cannot be resolved with conventional light microscopy, an interior including both monomers and short filaments is consistent with the diffuse fluorescence signal we observe. The aforementioned mechanisms of peripheral localization all depend on F-actin length. As such, the presence of short filaments in the interior does not qualitatively distinguish between them. Understanding how peripheral localization is regulated will be an exciting avenue for future studies.

Mechanism of actin assembly enhancement

The assembly of actin within coacervates for global actin concentrations below the critical concentration is largely predicted by the 30-fold increase in the local actin concentration via localization into the coacervate phase. Assuming that the measured RAM_{Int} corresponds primarily to monomer, we calculate the concentrations at which filament assembly within coacervates is expected and find that partitioning is sufficient to explain filament assembly down to 0.05 μM (*red dashed line*; Fig. 4 *F*). However, our measured partitioning is not quite sufficient to polymerize actin within coacervates at the lowest concentration (0.01 μM), yet we observe strong peripheral intensity (and interpret this to be polymerized actin). It is possible that the coacervate environment may alter the reaction rate kinetics of actin assembly (47,48), as has been seen for transcription in cell-lysate coacervates (49). Indeed, because the coacervate-phase volume fraction (40%) and viscosity (2 Pa-s) are similar to those of the cytoplasm, this system may serve as a useful platform to study biochemical reactions in a more physiological environment.

Implications for biochemical reaction regulation

The high local concentrations generated by partitioning provide for an elegant means to both spatially localize and enhance the rates of biochemical reactions. Spontaneous partitioning to a condensed liquid-like phase substantially reduces the quantities of protein needed to study reactions under more physiological conditions. Of particular interest is the possibility of having direct control over partition coefficients and other local physicochemical properties of the coacervate phase as a means to control biochemical reactivity.

In summary, we have illustrated spontaneous partitioning of proteins inside coacervate droplets, leading to markedly increased actin assembly rates and spatial confinement of filaments. Assembly rate enhancements reported here are qualitatively consistent with a model in which these enhancements were contributed to by an increase in the local effective concentration of actin monomers in the coacervate phase. Our work introduces exciting avenues for the use of synthetic polymers to control physical and biological properties of bioreactors, and address questions in biology about the biochemistry of molecules in cell-like microenvironments.

SUPPORTING MATERIAL

Supporting Materials and Methods, six figures, one table, and two movies are available at http://www.biophysj.org/biophysj/supplemental/S0006-3495(18)30251-0.

AUTHOR CONTRIBUTIONS

S.L.P. and M.L.G. conceived the project. P.M.M., S.S., S.L.P., D.R.K., M.L.G., and M.V.T. designed experiments. P.M.M., S.S., and S.L.P. performed experiments. D.R.K., M.L.G., and M.V.T. contributed essential reagents. P.M.M. analyzed image data and contributed analytical tools. P.M.M. and S.S. analyzed kinetic data. P.M.M. and S.S. performed physical estimates and calculations. P.M.M. prepared figures. P.M.M., S.S., and M.L.G. wrote the article with input from all authors.

ACKNOWLEDGMENTS

The authors thank C. Suarez, K. Weirich, T. Witten, J. Vieregg, K. Ishihara, and J. Löber, as well as the Gardel, Kovar, and Tirrell labs, for helpful discussion and suggestions. We thank L. Li for assistance with gel permeation chromatography measurements.

This work was primarily supported by the University of Chicago Materials Research Science and Engineering Center, which is funded by the National Science Foundation under award DMR-1420709. P.M.M. thanks the University of Chicago MRSEC for a graduate fellowship.

SUPPORTING CITATIONS

References (50–63) appear in the Supporting Material.

REFERENCES

1. Alberts, B., A. Johnson, …, P. Walter. 2007. Molecular Biology of the Cell, 5th Ed. Garland Science, New York.
2. Brangwynne, C. P., C. R. Eckmann, …, A. A. Hyman. 2009. Germline P granules are liquid droplets that localize by controlled dissolution/condensation. *Science.* 324:1729–1732.
3. Mitrea, D. M., and R. W. Kriwacki. 2016. Phase separation in biology; functional organization of a higher order. *Cell Commun. Signal.* 14:1.
4. Banani, S. F., A. M. Rice, …, M. K. Rosen. 2016. Compositional control of phase-separated cellular bodies. *Cell.* 166:651–663.
5. Feric, M., N. Vaidya, …, C. P. Brangwynne. 2016. Coexisting liquid phases underlie nucleolar subcompartments. *Cell.* 165:1686–1697.
6. van der Gucht, J., E. Spruijt, …, M. A. Cohen Stuart. 2011. Polyelectrolyte complexes: bulk phases and colloidal systems. *J. Colloid Interface Sci.* 361:407–422.
7. Srivastava, S., and M. V. Tirrell. 2016. Polyelectrolyte complexation. *In* Advances in Chemical Physics. S. A. Rice and A. R. Dinner, eds. John Wiley & Sons, New York, pp. 499–544.
8. Black, K. A., D. Priftis, …, M. Tirrell. 2014. Protein encapsulation via polypeptide complex coacervation. *ACS Macro Lett.* 3:1088–1091.
9. de Kruif, C. G., F. Weinbreck, and R. de Vries. 2004. Complex coacervation of proteins and anionic polysaccharides. *Curr. Opin. Colloid Interface Sci.* 9:340–349.
10. Lindhoud, S., and M. M. Claessens. 2016. Accumulation of small protein molecules in a macroscopic complex coacervate. *Soft Matter.* 12:408–413.
11. Martin, N., M. Li, and S. Mann. 2016. Selective uptake and refolding of globular proteins in coacervate microdroplets. *Langmuir.* 32:5881–5889.
12. Kim, M., S. J. Yeo, …, D. Lee. 2015. One-step generation of multifunctional polyelectrolyte microcapsules via nanoscale interfacial complexation in emulsion (NICE). *ACS Nano.* 9:8269–8278.
13. Zhao, M., S. A. Eghtesadi, …, N. S. Zacharia. 2017. Partitioning of small molecules in hydrogen-bonding complex coacervates of poly(acrylic acid) and poly(ethylene glycol) or pluronic block copolymer. *Macromolecules.* 50:3818–3830.
14. Liu, Y., H. H. Winter, and S. L. Perry. 2017. Linear viscoelasticity of complex coacervates. *Adv. Colloid Interface Sci.* 239:46–60.

15. Aumiller, W. M., Jr., and C. D. Keating. 2016. Phosphorylation-mediated RNA/peptide complex coacervation as a model for intracellular liquid organelles. *Nat. Chem.* 8:129–137.

16. Koga, S., D. S. Williams, …, S. Mann. 2011. Peptide-nucleotide microdroplets as a step towards a membrane-free protocell model. *Nat. Chem.* 3:720–724.

17. Pacalin, N. M., L. Leon, and M. Tirrell. 2016. Directing the phase behavior of polyelectrolyte complexes using chiral patterned peptides. *Eur. Phys. J. Spec. Top.* 225:1805–1815.

18. Perry, S. L., L. Leon, …, M. Tirrell. 2015. Chirality-selected phase behaviour in ionic polypeptide complexes. *Nat. Commun.* 6:6052.

19. Tanaka, F. 2011. Polymer Physics: Applications to Molecular Association and Thermoreversible Gelation. Cambridge University Press, Cambridge, United Kingdom.

20. Mohapatra, L., T. J. Lagny, …, J. Kondev. 2017. The limiting-pool mechanism fails to control the size of multiple organelles. *Cell Syst.* 4:559–567.e14.

21. Ou, Z., and M. Muthukumar. 2006. Entropy and enthalpy of polyelectrolyte complexation: Langevin dynamics simulations. *J. Chem. Phys.* 124:154902.

22. Priftis, D., R. Farina, and M. Tirrell. 2012. Interfacial energy of polypeptide complex coacervates measured via capillary adhesion. *Langmuir.* 28:8721–8729.

23. Brangwynne, C. P., T. J. Mitchison, and A. A. Hyman. 2011. Active liquid-like behavior of nucleoli determines their size and shape in *Xenopus laevis* oocytes. *Proc. Natl. Acad. Sci. USA.* 108:4334–4339.

24. ProtParam. ExPASy - ProtParam tool. http://web.expasy.org/protparam/ [Accessed April 21, 2017].

25. Vandekerckhove, J., A. Deboben, …, T. Wieland. 1985. The phalloidin binding site of F-actin. *EMBO J.* 4:2815–2818.

26. Tang, J. X., and P. A. Janmey. 1996. The polyelectrolyte nature of F-actin and the mechanism of actin bundle formation. *J. Biol. Chem.* 271:8556–8563.

27. Cooper, J. A., S. B. Walker, and T. D. Pollard. 1983. Pyrene actin: documentation of the validity of a sensitive assay for actin polymerization. *J. Muscle Res. Cell Motil.* 4:253–262.

28. Sept, D., and J. A. McCammon. 2001. Thermodynamics and kinetics of actin filament nucleation. *Biophys. J.* 81:667–674.

29. Bubb, M. R., L. Govindasamy, …, R. McKenna. 2002. Polylysine induces an antiparallel actin dimer that nucleates filament assembly: crystal structure at 3.5-Å resolution. *J. Biol. Chem.* 277:20999–21006.

30. Brown, S. S., and J. A. Spudich. 1979. Nucleation of polar actin filament assembly by a positively charged surface. *J. Cell Biol.* 80:499–504.

31. Oriol-Audit, C. 1978. Polyamine-induced actin polymerization. *Eur. J. Biochem.* 87:371–376.

32. Pollard, T. D. 1986. Rate constants for the reactions of ATP- and ADP-actin with the ends of actin filaments. *J. Cell Biol.* 103:2747–2754.

33. Fujiwara, I., D. Vavylonis, and T. D. Pollard. 2007. Polymerization kinetics of ADP- and ADP-Pi-actin determined by fluorescence microscopy. *Proc. Natl. Acad. Sci. USA.* 104:8827–8832.

34. Nolles, A., A. H. Westphal, …, J. W. Borst. 2015. Encapsulation of GFP in complex coacervate core micelles. *Biomacromolecules.* 16:1542–1549.

35. Obermeyer, A. C., C. E. Mills, …, B. D. Olsen. 2016. Complex coacervation of supercharged proteins with polyelectrolytes. *Soft Matter.* 12:3570–3581.

36. Vieregg, J. R., and T.-Y. D. Tang. 2016. Polynucleotides in cellular mimics: coacervates and lipid vesicles. *Curr. Opin. Colloid Interface Sci.* 26:50–57.

37. Kakran, M., and M. N. Antipina. 2014. Emulsion-based techniques for encapsulation in biomedicine, food and personal care. *Curr. Opin. Pharmacol.* 18:47–55.

38. Zhang, R., and B. I. Shklovskii. 2005. Phase diagram of solution of oppositely charged polyelectrolytes. *Phys. Stat. Mech. Its Appl.* 352:216–238.

39. Pak, C. W., M. Kosno, …, M. K. Rosen. 2016. Sequence determinants of intracellular phase separation by complex coacervation of a disordered protein. *Mol. Cell.* 63:72–85.

40. McCullough, B. R., E. E. Grintsevich, …, E. M. De La Cruz. 2011. Cofilin-linked changes in actin filament flexibility promote severing. *Biophys. J.* 101:151–159.

41. Kuhn, J. R., and T. D. Pollard. 2005. Real-time measurements of actin filament polymerization by total internal reflection fluorescence microscopy. *Biophys. J.* 88:1387–1402.

42. Murrell, M. P., and M. L. Gardel. 2012. F-actin buckling coordinates contractility and severing in a biomimetic actomyosin cortex. *Proc. Natl. Acad. Sci. USA.* 109:20820–20825.

43. Asakura, S., and F. Oosawa. 1954. On interaction between two bodies immersed in a solution of macromolecules. *J. Chem. Phys.* 22:1255–1256.

44. de Gennes, P.-G. 1979. Scaling Concepts in Polymer Physics, 1st Ed. Cornell University Press, Ithaca, NY.

45. Andelman, D., and J.-F. Joanny. 2000. Polyelectrolyte adsorption. *Comptes Rendus Acad. Sci. IV Phys.* 1:1153–1162.

46. Bon, S. A. F. 2014. The phenomenon of Pickering stabilization: a basic introduction. *In* Particle-Stabilized Emulsions and Colloids. S. A. F. Bon and T. Ngai, eds. Royal Society of Chemistry Publishing, Cambridge, United Kingdom, pp. 1–7.

47. Drenckhahn, D., and T. D. Pollard. 1986. Elongation of actin filaments is a diffusion-limited reaction at the barbed end and is accelerated by inert macromolecules. *J. Biol. Chem.* 261:12754–12758.

48. Frederick, K. B., D. Sept, and E. M. De La Cruz. 2008. Effects of solution crowding on actin polymerization reveal the energetic basis for nucleotide-dependent filament stability. *J. Mol. Biol.* 378:540–550.

49. Sokolova, E., E. Spruijt, …, W. T. Huck. 2013. Enhanced transcription rates in membrane-free protocells formed by coacervation of cell lysate. *Proc. Natl. Acad. Sci. USA.* 110:11692–11697.

50. Kramer, J. R., and T. J. Deming. 2010. General method for purification of α-amino acid-*n*-carboxyanhydrides using flash chromatography. *Biomacromolecules.* 11:3668–3672.

51. Spudich, J. A., and S. Watt. 1971. The regulation of rabbit skeletal muscle contraction. I. biochemical studies of the interaction of the tropomyosin-troponin complex with actin and the proteolytic fragments of myosin. *J. Biol. Chem.* 246:4866–4871.

52. Kovar, D. R., J. R. Kuhn, …, T. D. Pollard. 2003. The fission yeast cytokinesis formin Cdc12p is a barbed end actin filament capping protein gated by profilin. *J. Cell Biol.* 161:875–887.

53. Kudryashov, D. S., and E. Reisler. 2003. Solution properties of tetramethylrhodamine-modified G-actin. *Biophys. J.* 85:2466–2475.

54. Hansen, S., J. B. Zuchero, and R. D. Mullins. 2013. Cytoplasmic actin: purification and single molecule assembly assays. *In* Adhesion Protein Protocols. A. S. Coutts, ed. Humana Press, New York, NY, pp. 145–170.

55. Molecular Probes. The Molecular Probes Handbook. https://www.thermofisher.com/us/en/home/references/molecular-probes-the-handbook.html [Accessed April 21, 2017].

56. Winkelman, J. D., C. G. Bilancia, …, D. R. Kovar. 2014. Ena/VASP Enabled is a highly processive actin polymerase tailored to self-assemble parallel-bundled F-actin networks with Fascin. *Proc. Natl. Acad. Sci. USA.* 111:4121–4126.

57. Jönsson, P., M. P. Jonsson, …, F. Höök. 2008. A method improving the accuracy of fluorescence recovery after photobleaching analysis. *Biophys. J.* 95:5334–5348.

58. Shimozawa, T., K. Yamagata, …, Y. Mimori-Kiyosue. 2013. Improving spinning disk confocal microscopy by preventing pinhole cross-talk for intravital imaging. *Proc. Natl. Acad. Sci. USA.* 110:3399–3404.

59. Pubchem. L-glutamic acid | C5H9NO4 - PubChem. https://pubchem.ncbi.nlm.nih.gov/compound/L-glutamic_acid [Accessed May 8, 2017].

60. Spruijt, E., A. H. Westphal, …, J. van der Gucht. 2010. Binodal compositions of polyelectrolyte complexes. *Macromolecules.* 43:6476–6484.

61. Hanke, F., A. Serr, …, R. R. Netz. 2010. Stretching single polypeptides: the effect of rotational constraints in the backbone. *EPL Europhys. Lett.* 92:53001.

62. Dobrynin, A. V. 2005. Electrostatic persistence length of semiflexible and flexible polyelectrolytes. *Macromolecules.* 38:9304–9314.

63. Carrion-Vazquez, M., A. F. Oberhauser, …, J. M. Fernandez. 1999. Mechanical and chemical unfolding of a single protein: a comparison. *Proc. Natl. Acad. Sci. USA.* 96:3694–3699.

Biophysical Journal, Volume *114*

Supplemental Information

Partitioning and Enhanced Self-Assembly of Actin in Polypeptide Coacervates

Patrick M. McCall, Samanvaya Srivastava, Sarah L. Perry, David R. Kovar, Margaret L. Gardel, and Matthew V. Tirrell

SUPPORTING MATERIAL

Partitioning and Enhanced Self-Assembly of Actin in Polypeptide Coacervates

Patrick M. McCall,[a,b,1,2] Samanvaya Srivastava,[c,d,1,3] Sarah L. Perry,[c,4] David R. Kovar,[e,f] Margaret L. Gardel,[a,b,g,5,6] and Matthew V. Tirrell[c,d,5,6]

[a]*Department of Physics,* [b]*James Franck Institute,* [c]*Institute for Molecular Engineering,* [e]*Department of Molecular Genetics and Cell Biology,* [f]*Department of Biochemistry and Molecular Biology and* [g]*Institute for Biophysical Dynamics, The University of Chicago, Chicago, IL 60637, USA*

[d]*Argonne National Laboratory, Argonne, IL 60439, USA*

Footnotes:

[1] These authors contributed equally to this work.

[2] Current address: Max Planck Institute of Molecular Cell Biology and Genetics, Pfotenhauerstraße 108, 01307 Dresden, Germany

[3] Current address: Department of Chemical and Biomolecular Engineering, University of California, Los Angeles, Los Angeles, CA 90095, USA

[4] Current address: Department of Chemical Engineering, University of Massachusetts Amherst, Amherst, MA, 01003, USA

[5] These authors contributed equally to this work.

[6] To whom correspondence may be addressed. Email: gardel@uchicago.edu, or mtirrell@uchicago.edu.

SUPPORTING MATERIAL CONTENTS:

I. SUPPLEMENTAL MATERIALS AND METHODS

I.a. Polypeptide Synthesis and Storage

The racemic polyanion poly(L,D)-glutamate sodium salt (pRE) was purchased from Alamanda Polymers Inc. This is a 50/50 random copolymer of L- and D-glatamate stereoisomers. Poly(L-lysine hydrochloride) (pLK) was purchased from Alamanda Polymers Inc. or prepared in-house via N-carboxyanhydride (NCA) polymerization and characterized using gel permeation chromatography (GPC) and ^{1}H NMR (1). See Table S1 for the source, mean degree of polymerization, molecular weight, polydispersity, for the polypeptides used in each Figure.

Stock solutions were prepared gravimetrically using MilliQ water (resistivity of 18.2 MΩ-cm, Millipore) at concentrations of either 10 or 20 mM with respect to the number of monomers (that is, the number of acid or base groups) present in solution and then adjusted to pH 7.0 using concentrated solutions of HCl and NaOH, as needed. These solutions were stored at 4 °C, and wrapped in parafilm to minimize evaporation. Unless otherwise noted, peptide concentrations are reported in terms of charge equivalents. For instance, a concentration of 5 mM pLK indicates a 5 mM concentration of lysine residues, each with an average charge equivalent of +1 at pH 7. Correspondingly, the concentration of pLK molecules is 50 μM, with each pLK molecule composed of, on average, 100 +1-charged lysine residues.

I.b. Protein Purification, Labeling, and Storage

Actin was purified from rabbit skeletal muscle acetone powder (Pel-Freez) as previously described (2). A subset of gel-filtered actin was labeled on Cys-347 with either Oregon green 488 iodoacetamide (OG), Tetramethylrhodamine-5-maleimide (TMR), or pyrenyl iodoacetamide (Invitrogen) (3–5). All actins were stored in Calcium Buffer-G (CaBG: 2 mM Tris-HCl, pH 8.0 at 22 °C, 0.2 mM ATP (adenosine triphosphate), 0.5 mM DTT (1,4-Dithiothreitol), 0.1 mM $CaCl_2$, 1 mM NaN_3). Unlabeled, OG- and pyrene-labeled actins were stored at 4 °C, while TMR-labeled actin was flash-frozen with liquid nitrogen and stored at -80 °C. Prior to use, non-frozen actins were dialyzed against 0.2 L fresh CaBG for 18-24 h, and clarified via ultracentrifugation at 177,000 x g (average relative centrifugal force) for 30 minutes at 4 °C. The top 90% of the supernatant was retained, stored on ice, and used within 6 days. TMR-actin was rapidly thawed by hand, and similarly clarified via ultracentrifugation at 177,000 x g for 30 minutes at 4 °C. The top 75% of the supernatant was retained, stored on ice, and used within 2 days.

Bovine Serum Albumin (BSA) (Fraction V, Fisher Scientific) was labeled on exposed cysteines with Alexa Fluor 647 Maleimide (Invitrogen) according to the manufacturer's protocol, and stored in 1x Phosphate-Buffered Saline (PBS, pH 7.5 at room temperature) at -80 °C. Prior to use, labeled BSA was thawed rapidly by hand, and clarified by centrifugation at 21,000 x g for 20 minutes at 4 °C. The entire supernatant was retained, stored at 4 °C, and used within one month.

I.c. Protein Concentration Determination

Protein concentrations were determined spectrophotometrically. Absorbance measurements were made using an Ultrospec 2100 pro (Amersham Biosciences) or a NanoDrop ND-1000 (Thermo Scientific) UV/VIS Spectrophotometer with optical path lengths b = 1 cm and b = 0.1 cm, respectively. Sample absorbance was converted to protein concentration (and corrected for label absorbance, as appropriate) using the following expressions:

[Unlabeled-actin] = $\langle A_{290} \rangle$ *(38.5 µM cm) / b (6)

For OG-labeled actin (5):

[Total actin] = ($\langle A_{290} \rangle$ - (0.17*$\langle A_{491} \rangle$))*(38.5 µM cm) / b

[OG-actin] = $\langle A_{491} \rangle$ / ((0.0778 μM^{-1} cm^{-1})*b)

For TMR-labeled actin:

[Total actin] = ($\langle A_{290} \rangle$ - (0.1185* $\langle A_{557} \rangle$))*(38.5 µM cm) / b

[TMR-actin] = $\langle A_{557} \rangle$ / ((0.1009 μM^{-1} cm^{-1})*b)

For Pyrene-labeled actin (6):

[Total actin] = ($\langle A_{290} \rangle$ - (0.127*$\langle A_{344} \rangle$))*(38.5 µM cm) / b

[Pyrene-actin] = $\langle A_{344} \rangle$*(45.0 µM cm) / b

For BSA, the molar extinction coefficient was estimated to be E_{280} = 40,800 M^{-1} cm^{-1} using the online tool ProtParam (http://web.expasy.org/protparam/), the amino acid sequence associated with the UniProt ID P02769 for *Bos taurus* serum albumin, and assuming reduced Cys residues. The approximate extinction coefficient for Alexa Fluor 647 C_2 maleimide is E_{650} = 265,000 M^{-1} cm^{-1} (7). The concentration of BSA and Alexa Fluor 647 were thus calculated according to:

[Total BSA] = ($\langle A_{280} \rangle$ -(0.03*$\langle A_{651} \rangle$)) / ((0.0408 μM^{-1} cm^{-1})*b)

[Alexa 647] = $\langle A_{651} \rangle$ / ((0.265 μM^{-1} cm^{-1})*b)

I.d. Sample Preparation

Mg-ATP-actin is prepared in Tube A from Ca-ATP-actin by 2-minute incubation at room temperature (RT) with 1/10th volume 10x Magnesium Exchange buffer (1x ME buffer: 50 µM $MgCl_2$, 200 µM EGTA (ethylene glycol-bis(beta-aminoethyl ether)-N,N,N',N'-tetraacetic acid) in MilliQ-purified water, stored at RT). Mg-ATP-actin is then incubated at RT with either Latrunculin A dissolved in DMSO (dimethyl sulfoxide) for 5 min or an equivalent volume of DMSO, as a blank, for minimal time (< 30 s), followed by addition of pLK (or a blank of MilliQ-purified water) and incubation for 2-3 min at RT. Tube B is assembled from 10x KMEI buffer (1x KMEI: 50 mM KCl, 1 mM $MgCl_2$, 1 mM EGTA, 10 mM Imidazole, pH 7.0, stored at RT), Magnesium Buffer-G (MgBG: 2 mM Tris-HCl, pH 8.0, 22 °C, 0.2 mM ATP, 0.5 mM DTT, 0.1 mM $MgCl_2$, 1 mM NaN_3, stored on ice), and pRE (or a blank of MilliQ-purified water). Polyelectrolyte phase separation and actin polymerization is then initiated simultaneously through the addition of Tube B to Tube A and rapid mixing by pipette. Samples with ~ 1 mM or more total polypeptide are visibly turbid < 2 s after addition of Tube B to Tube A.

I.e. Microscopy

Samples were loaded into flow cells constructed from mPEG-Silane-treated glass and double-sided tape, as described previously (8). Samples were imaged at room temperature (~24 °C) on an inverted microscope (Ti-Eclipse; Nikon, Melville, NY) equipped with a confocal scan head (CSU-X, Yokogawa Electric, Musashino, Tokyo, Japan), a laser merge module (LMM5, Spectral Applied Research, Richmond Hill, Ontario, Canada) containing 488-nm, 560-nm, and 635-nm laser lines for fluorescence imaging, as well as polarizers, Nemarski prisms, and a white transmitted-light source for differential interference contrast (DIC) imaging. A 405-nm laser line was used as an excitation source for photobleaching experiments. The location of the bleached region was controlled with a micromirror array (MOSAIC, Photonics Instruments). Images were formed using a 60x, DIC-compatible, water-immersion objective (Nikon, Melville, NY) with a numerical aperature (NA) of 1.2, and corrections for apochromatic and flat field aberrations (Plan Apo). Images were acquired on a scientific complementary metal-oxide-semiconductor (sCMOS) camera (Zyla 4.2; Andor Technologies, Belfast, Northern Ireland), with a physical pixel size of 6.5 microns per side. All imaging hardware was controlled using METAMORPH acquisition software (Molecular Devices, Eugene, OR).

I.f. Image Analysis

All quantitative image analysis was performed using imageJ (NIH, imagej.nih.gov/ij/) and custom code written in MATLAB (MathWorks, Natick, MA). Camera dark noise (100 counts) was subtracted from all fluorescence images prior to analysis.

I.f.1. Measurement of average relative accumulated mass (RAM) in Figure 1E, S3, and S4. Following camera noise subtraction, fluorescence images were corrected for uneven illumination (9) using a reference fluorescence image of a plastic slide. Two masks were created for each corrected fluorescence image by thresholding. The first is called the background mask, and the second is called the droplet mask. Note that in order to reduce the impact of imaging artifacts which result from spinning-disk confocal imaging, such as pin-hole crosstalk, the background mask is not simply the inverse of the droplet mask (10, 11). We used the modal pixel intensity from the illumination-corrected fluorescence image as the threshold for the background mask. After application of the threshold, the close, invert, close, and fill holes operations were applied in ImageJ. This procedure yields a mask which excludes droplets, as well as regions outside of droplets where systematic pin-hole cross-talk effects are visible.

To create the droplet mask, the illumination-corrected image was thresholded again, this time using the average full-width-at-half-max intensity obtained from line scans across 5-10 coacervate droplets in the field of view. After application of the threshold, the invert, close, fill holes, and invert operations were applied in ImageJ.

Individual candidate droplets were then automatically identified from the droplet mask using custom code written in MATLAB. Candidate droplets were filtered by size and eccentricity. As a result of the strong peripheral localization of actin fluorescence, candidate droplets occasionally had a crescent-like morphology, similar to an unclosed circle. This occurred if the fluorescence

at some position along the droplet boundary was below the masking threshold. To remove droplets for which the mask gave unclosed circles, candidate droplets in actin fluorescence images were further filtered by removing candidates for which the center of mass fell outside the candidate droplet region. The size and average intensity of each filtered droplet was then computed using the droplet mask and the illumination-corrected fluorescence image. The average background intensity was computed using the background mask and the illumination-corrected image. Finally, the average partition coefficient for each droplet was calculated as the ratio of the average intensity within the droplet mask to the average background intensity.

I.f.2. Measurement of peripheral and interior Relative Accumulated Mass values in Figure 4E. Fluorescence intensity line scans are calculated using a transverse width of 5 pixels along paths indicated in the accompanying image, and normalized according to

$$I_{\mathrm{norm}}(x) = \left(I(x) - I_{\mathrm{min}}\right) / \left(I_{\mathrm{max}} - I_{\mathrm{min}}\right) \quad (1)$$

where *I(x)* is the intensity at position *x* along the path, and I_{min} and I_{max} are the minimum and maximum values of the intensity along the path, respectively. Interior, Periphery, and Exterior fluorescence values (e.g. Fig. 4F) are obtained from individual line scans. Interior is the average of a 5-pixel segment along the line scan, co-centered with the droplet. Periphery is the average of the maximum intensity along the line scan from either side of the droplet center. Exterior signal is calculated on each side of the droplet as the average intensity along the 6-pixel segment of the line scan extending from 10 pixels beyond the periphery peak to 15 pixels beyond the peak. The reported Exterior value is the average of the Exterior signals from each side of the line scan. One-sided Exterior values (as opposed to the average of both sides) are reported when the relevant segment on one side of the line scan impinges upon an adjacent droplet. Line scan orientation is chosen to minimize the frequency of this. These auxiliary RAM values are calculated as the ratio of either Periphery or Interior fluorescence to Exterior fluorescence.

I.f.3. Measurement of fluorescence intensity correlation coefficients. Calculation of fluorescence intensity correlation coefficients is restricted to include only pixels within droplets using a mask for each field of view. Masks were generated in ImageJ from DIC images taken at the approximate midplane of the droplet of interest by application of a Gaussian blur (radius 1.00), threshold-based conversion to a binary image, and the sequential application of the binary operations close, fill holes, and dilate, where dilate is applied twice. The intensities in the fluorescence cross-correlation histogram (e.g. Fig. 2C) are normalized independently in each channel according to equation (1) above, where the domain of *x* is all pixels identified from the mask as within droplets.

I.f.4. Measurement of fluorescence recovery after photobleaching (FRAP)

Following acquisition of pre-bleach images, photobleaching was performed by illuminating a rectangular region of interest (ROI) encompassing one or more coacervate droplets with a 405-nm laser for 5 seconds using a MOSAIC micromirror array. Camera dark noise (100 counts) was subtracted from all fluorescence images prior to analysis. The average fluorescence intensity of the bleached region is normalized according to:

$$\tilde{I}_{\text{spot}}(t) = \frac{I_{\text{spot}}(t) - I_{\text{spot}}(t_{bleach})}{I_{\text{spot}}(t_0) - I_{\text{spot}}(t_{bleach})} \quad (2)$$

where t_{bleach} is the first post-bleach frame, t_0 is the first frame acquired, and $I(t)$ is the average fluorescence intensity of the bleached region following subtraction of camera noise.

Additional, unwanted photobleaching inevitably occurs during fluorescence imaging. The timecourse of this bleaching is approximated by the decay of the fractional average fluorescence of a control droplet of the same size at time t:

$$f_{Photobleaching} = \frac{I_{\text{control}}(t)}{I_{\text{control}}(t_0)} \quad (3)$$

Note that $f_{Photobleaching}$ is unity at t_0, and decays monotonically to between 0.6 and 0.7 over 4 minutes. To account for this imaging-derived photobleaching, the normalized intensity (2) is divided by the fractional average fluorescence remaining:

$$\tilde{I}_{\text{spot,PBC}}(t) = \frac{\tilde{I}_{\text{spot}}(t)}{f_{Photobleaching}} \ . \quad (4)$$

It is this photobleach-corrected, normalized spot intensity, $\tilde{I}_{\text{spot,PBC}}(t)$, that is plotted as the FRAP recovery in Fig. S5.

I.g. Fluorescence Spectroscopy

A stock solution of 15 µM Ca-ATP-actin (typically 10-20 % pyrene-labeled) is prepared from solutions of unlabeled and highly-labeled (typically > 90 %) actin in a 1.5-mL microcentrifuge tube, and then converted from Ca-ATP-actin by 2-minute incubation with 1/10th volume 10x ME buffer and 1/10th volume of 100x anti-foam (Antifoam 204, Sigma) at RT. Mg-ATP-actin is then incubated with the desired concentration of pLK (or a blank of MilliQ-purified water) for 2-3 min at RT in up to 12 rows of a 96-well plate (Assay Plate 3686, Corning). A multichannel pipette is then used to simultaneously deliver solution assembled from 10x KMEI buffer MgBG, and pRE (or a blank of MilliQ-purified water) to the wells containing actin, thereby initiating assembly (through the addition of $MgCl_2$ and KCl) and phase separation (through the addition of the polyanion) simultaneously. The final reaction volume is 150 µL. Actin assembly is monitored at RT by pyrene fluorescence (Excitation: 365 nm, Emission: 407 nm) in a fluorescence plate reader (Saphire2, Tecan). The timecourse of pyrene excimer fluorescence (Excitation: 343 nm, Emission: 478 nm (12) was monitored concomitantly with assembly by sequentially alternating the excitation/emission wavelength pairs on a fluorescence plate reader (Infiniti m200, Tecan). We report the reciprocal of the time to 50 %-assembly ($1/t_{1/2}$) as a measure of the mean assembly rate. $t_{1/2}$ is determined for each 407-nm fluorescence timecourse as the time-point at which the fluorescence intensity is closest to $I_{1/2}$, which is defined as

$$I_{1/2} = \left(I_{\max} + I_0\right)/2 \quad (5)$$

where I_{max} is the maximum intensity of the timecourse, and I_0 is the initial fluorescence value of the actin-only control sample, which is an estimate of the sum of background contributions from the detector, buffers, and pyrene-actin monomers for all conditions.

I.h. Physical Estimates

I.h.1. Estimation of osmotic pressure required to crowd F-actin to an interface. We estimate the minimum osmotic pressure needed to crowd F-actin to an interface as that of a 0.25 % (w/v) methylcellulose solution, which is known to be sufficient (13). Using the van 't Hoff formula $\Pi = cN_A k_B T$ for the osmotic pressure of a dilute polymer at molar concentration c, where N_A is Avagadro's number, we find that a concentration of $c = 0.25\% \cong 180\ \mu M$ of 14-kDa methylcellulose gives a pressure of $\Pi^* \cong 450$ Pa at room temperature.

I.h.2. Estimation of polypeptide species concentration in dilute phase. The dilute phase concentration of a polypeptide is the critical concentration for phase separation at that temperature and salt concentration. Thus, observation of droplet formation upon mixing of pLK with pRE, each at a final global concentration X, indicates that X is greater than the critical concentration, and thereby greater than the dilute phase concentration. pLK/pRE coacervate droplets are visible by DIC at concentrations of 30 μM per polypeptide and above. However, punctate BSA fluorescence is observed at 3 μM per polypeptide, even though droplets are not readily discernible by DIC. This suggests that phase separation does still occur at this concentration. We thus use 3000 nM / 100 residues per polypeptide = 30 nM as a conservative upper bound on the dilute phase concentration for each polypeptide chain species.

I.h.3. Estimation of polypeptide concentration in coacervate phase. From dimensional analysis, we estimate the polypeptide concentration in the coacervate phase from the mass fraction according to $c = \rho_{pp} f_{pp} / M_W$, where ρ_{pp} is the mass density of a solid polypeptide substance, f_{pp} is the polypeptide mass fraction in the coacervate phase, and M_W is the polypeptide molecular weight. We estimate the polypeptide mass density ρ_{pp} as the density of solid glutamic acid, ρ_E = 1538 mg/mL (14). Unpublished measurements of f_{pp} for pLK/pRE coacervates under similar conditions find a total polypeptide mass fraction of 0.38, or 0.19 per polypeptide species. This is comparable to previously published reports on other coacervate systems, where the water content was reported to saturate at ~ 60 % (15). Using these values, and approximating the molecular weight as 12.9 kDa (Table S1), yields a polypeptide chain concentration of ~2 mM per species, corresponding to a peptide concentration of ~ 2 M per species. In the main text, we thus report the pLK concentration estimate as being on the order of 1-3 M in the coacervate phase.

I.h.4. Estimation of coacervate mesh size. We estimate the mesh size as (16) $\xi = R_F \left(\Phi^*_{pp} / \Phi_{pp} \right)^{3/4}$, where R_F is the root-mean-square end-to-end distance of the polypeptide, Φ^*_{pp} is the polypeptide volume fraction at which spheres of radius R_F containing one polymer each begin to overlap, and Φ_{pp} is the polypeptide volume fraction of the coacervate phase. Treating the polypeptides as self-avoiding flexible chains in good solvent, we have that (16)

$R_F = aN^{\nu} = aN^{3/5}$, where a is the effective monomer size of the self-avoiding chain, N is the number of such monomers per chain, and ν is the Flory exponent. We also have that $\Phi^*_{pp} \cong c^* a^3 = \frac{N}{R_F{}^3} a^3 = N^{-4/5}$, where c^* is the overlap polymer concentration. Combining these expressions gives (16) $\xi = a\Phi_{pp}{}^{-3/4}$.

We take the effective monomer size of a polypeptide in the coacervate phase to be the Kuhn length, which we estimate as (17) 0.8 +/- 0.1 nm. We estimate the volume fraction as

$$\Phi_{pp} = \frac{f_{pp}}{f_{pp} + \left(1 - f_{pp}\right)\frac{\rho_{pp}}{\rho_{\text{solvent}}}}. \quad (6)$$

Taking the total polypeptide mass fraction to be f_{pp} = 0.38 as above, and approximating ρ_{solvent} as 1000 mg/mL, we estimate the volume fraction as Φ_{pp} = 0.28. Combined with the Kuhn length estimate, this gives a mesh size estimate of ~2.1 nm. In the main text, we estimate the mesh-size as 2-3 nm in the coacervate phase.

I.h.5. Estimation of polyelectrolyte flexibility in coacervate phase. For polyelectrolytes, the total persistence length l_T can be defined by the sum of a backbone or "bare" persistence length, l_0, which derives from the chemical structure of the chain, and an electrostatic persistence length, l_E, determined by electrostatic interactions, yielding $l_T = l_0 + l_E$ (18). For the backbone persistence length, there is some uncertainty in estimating valued for pLK and pRE from the literature. Single-molecule force spectroscopy measurements of Ig-repeats from the protein titin found $l_0 = 3.9 \pm 0.1$ Å by fitting force extension curves to a worm-like chain model (19). Depending on model assumptions, analytic and numerical calculations for polyglycine give persistence lengths between 3.18 and 4.47 Å (17). We chose a value of 3.9 Å to match experiments for titin Ig domains, and which is within 20% of both the largest and the smallest model bounds.

The electrostatic persistence length can be defined as (18)

$$l_E = \frac{l_B f^2}{4\kappa^2 b^2}, \quad (7)$$

where l_B is the Bjerrum length, f is the fraction of monomers that have a charge on them, and b is the bond length of the polyelectrolyte. κ is the inverse of the Debye length, given by

$$\kappa^2 = 4\pi l_B \left[Z_c^2 c_c + \sum_\gamma Z_\gamma^2 c_\gamma \right], \quad (8)$$

where Z is the valency, c is the concentration of the ions present in the solution, and the subscripts c and γ correspond to the counterion associated with the polyelectrolyte and all the ion species contributed by the addition of salt, respectively. Combining Equations (7-8) gives

$$l_E = \frac{f^2}{16\pi \left[Z_c^2 c_c + \sum_\gamma Z_\gamma^2 c_\gamma \right] b^2}. \quad (9)$$

The electrostatic contribution is maximal in the dilute limit, where charged monomers primarily interact with and repel adjacent monomers, and in absence of added salts, which would screen electrostatic interactions. We therefore estimate the maximum persistence length for a fully charged polypeptide chain (*f = 1*) in this limit, where the sum over gamma vanishes. For a polypeptide, the bond length can be estimated as $b = 3.65\,\text{Å}$ (17). Plugging these values into Equation (9), and noting that 1 mol / L = 10^{-27} mol / Å^3, yields

$$l_E = \frac{1}{16\pi} \cdot \frac{10^{27}\,\text{Å}^3}{c_c N_A\ \text{mol}} \cdot \frac{1}{\left(3.65\,\text{Å}\right)^2} \cong \frac{2.48}{c_m}\,\text{Å}, \tag{10}$$

where c_c=c_m is the polyelectrolyte monomer concentration in units of mol / L.

Thus, in the absence of added salt in the medium (beyond counterions), we estimate the maximum persistence length of our polypeptide chains as $l_T = (2.48/c_m + 3.9)$ Å. In our pLK/pRE coacervates, we estimate $c_m \approx 2$ mol/L for each species (calculation is given above), and hence l_T = 5.14 Å. In the coacervate, however, the charge is strongly screened by both the residues from oppositely-charged chains (also at $c_m \approx 2$ mol/L) and ≈ 140 mM salt. Therefore, we expect the contribution from the electrostatic persistence length to be negligible, and the total persistence length to be essentially that of the intrinsic backbone persistence length. Therefore, we have used l_T = 0.4 nm and $b = 2l_T$ = 0.8 nm in our estimates in the manuscript.

Importantly, however, we note that the osmotic pressure required to crowd actin to a surface with a dilute solution of methylcellulose (estimated above as ≈ 450 Pa) is 3 orders of magnitude smaller than the osmotic pressure we estimate for the polypeptides in the coacervate. In terms of mesh size, the threshold for crowding is 20 nm, about an order of magnitude larger than the mesh size of 2.1 nm we quote in the section above. The mesh size is linear in the persistence length, so an order of magnitude error in the persistence length is necessary for the osmotic pressure of the pLK/pRE chains to fall below the crowding threshold. From our data, the electrostatic contribution to the polyelectrolyte rigidity is insufficient to account for this; using our lower bound monomer concentration c_m= 1 mol/L and still neglecting salt in order to maximize the persistence length only increases the mesh size to 5.8 nm.

I.i. Supporting References:

1. Kramer, J.R., and T.J. Deming. 2010. General Method for Purification of α-Amino acid-N-carboxyanhydrides Using Flash Chromatography. Biomacromolecules. 11: 3668–3672.

2. Spudich, J.A., and S. Watt. 1971. The Regulation of Rabbit Skeletal Muscle Contraction I. BIOCHEMICAL STUDIES OF THE INTERACTION OF THE TROPOMYOSIN-TROPONIN COMPLEX WITH ACTIN AND THE PROTEOLYTIC FRAGMENTS OF MYOSIN. J. Biol. Chem. 246: 4866–4871.

3. Kovar, D.R., J.R. Kuhn, A.L. Tichy, and T.D. Pollard. 2003. The fission yeast cytokinesis formin Cdc12p is a barbed end actin filament capping protein gated by profilin. J. Cell Biol. 161: 875–887.

4. Kudryashov, D.S., and E. Reisler. 2003. Solution Properties of Tetramethylrhodamine-Modified G-Actin. Biophys. J. 85: 2466–2475.

5. Kuhn, J.R., and T.D. Pollard. 2005. Real-Time Measurements of Actin Filament Polymerization by Total Internal Reflection Fluorescence Microscopy. Biophys. J. 88: 1387–1402.

6. Hansen, S., J.B. Zuchero, and R.D. Mullins. 2013. Cytoplasmic Actin: Purification and Single Molecule Assembly Assays. In: Coutts AS, editor. Adhesion Protein Protocols. Humana Press. pp. 145–170.

7. Molecular Probes. The Molecular Probes Handbook. Available at: https://www.thermofisher.com/us/en/home/references/molecular-probes-the-handbook.html [Accessed April 21, 2017].

8. Winkelman, J.D., C.G. Bilancia, M. Peifer, and D.R. Kovar. 2014. Ena/VASP Enabled is a highly processive actin polymerase tailored to self-assemble parallel-bundled F-actin networks with Fascin. Proc. Natl. Acad. Sci. 111: 4121–4126.

9. Jönsson, P., M.P. Jonsson, J.O. Tegenfeldt, and F. Höök. 2008. A Method Improving the Accuracy of Fluorescence Recovery after Photobleaching Analysis. Biophys. J. 95: 5334–5348.

10. Banani, S.F., A.M. Rice, W.B. Peeples, Y. Lin, S. Jain, R. Parker, and M.K. Rosen. 2016. Compositional Control of Phase-Separated Cellular Bodies. Cell. 166: 651–663.

11. Shimozawa, T., K. Yamagata, T. Kondo, S. Hayashi, A. Shitamukai, D. Konno, F. Matsuzaki, J. Takayama, S. Onami, H. Nakayama, Y. Kosugi, T.M. Watanabe, K. Fujita, and Y. Mimori-Kiyosue. 2013. Improving spinning disk confocal microscopy by preventing pinhole cross-talk for intravital imaging. Proc. Natl. Acad. Sci. 110: 3399–3404.

12. Bubb, M.R., L. Govindasamy, E.G. Yarmola, S.M. Vorobiev, S.C. Almo, T. Somasundaram, M.S. Chapman, M. Agbandje-McKenna, and R. McKenna. 2002. Polylysine Induces an Antiparallel Actin Dimer That Nucleates Filament Assembly CRYSTAL STRUCTURE AT 3.5-Å RESOLUTION. J. Biol. Chem. 277: 20999–21006.

13. Murrell, M.P., and M.L. Gardel. 2012. F-actin buckling coordinates contractility and severing in a biomimetic actomyosin cortex. Proc. Natl. Acad. Sci. 109: 20820–20825.

14. Pubchem. L-glutamic acid | C5H9NO4 - PubChem. Available at: https://pubchem.ncbi.nlm.nih.gov/compound/L-glutamic_acid [Accessed May 8, 2017].

15. Spruijt, E., A.H. Westphal, J.W. Borst, M.A. Cohen Stuart, and J. van der Gucht. 2010. Binodal Compositions of Polyelectrolyte Complexes. Macromolecules. 43: 6476–6484.

16. de Gennes, P.-G. 1979. Scaling Concepts in Polymer Physics. 1st ed. Ithaca, NY: Cornell University Press.

17. Hanke, F., A. Serr, H.J. Kreuzer, and R.R. Netz. 2010. Stretching single polypeptides: The effect of rotational constraints in the backbone. EPL Europhys. Lett. 92: 53001.

18. Dobrynin, A.V. 2005. Electrostatic Persistence Length of Semiflexible and Flexible Polyelectrolytes. Macromolecules. 38: 9304–9314.

19. Carrion-Vazquez, M., A.F. Oberhauser, S.B. Fowler, P.E. Marszalek, S.E. Broedel, J. Clarke, and J.M. Fernandez. 1999. Mechanical and chemical unfolding of a single protein: A comparison. Proc. Natl. Acad. Sci. 96: 3694–3699.

II. SUPPLEMENTAL TABLE

Polypeptide	Source	Degree of Polymerization	Molecular Weight (kDa)	Polydispersity	Experiments
pLK100	purchased	100	12.8	1.004	Fig. 1, 2, 3D, 4 Fig. S1, S2, S3, S4, S5
pLK126	in-house	126	16.2	1.30	Fig. 3B-C, S6
pRE100	purchased	100	12.9	1.15	Fig. 1, 2, 3D, 4 Fig. S1, S2, S3, S4, S5
pRE98	purchased	98	12.7	1.02	Fig. 3B-C, S6

Table S1. **Summary of polypeptides used in this study.**

III. SUPPLEMENTAL FIGURES

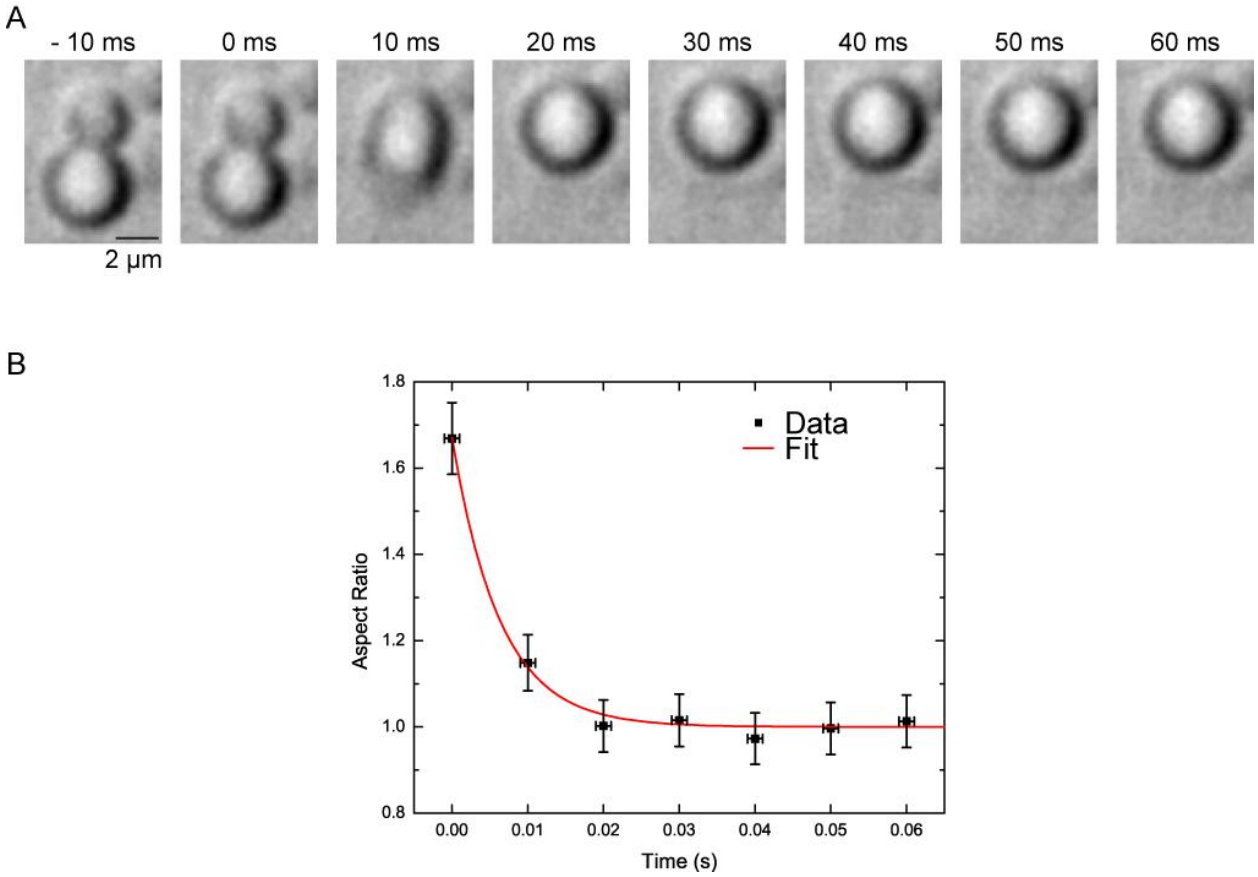

Figure S1. Liquid-like properties of pLK/pRE coacervates. (A) DIC microscopy time-lapse of two coacervates merging. Both droplets are initially round, suggestive of surface-tension dominated shapes. Upon fusing, the initially dumbbell-shaped interface rapidly relaxes to a round, surface-area-minimizing conformation of diameter d = 4 μm. (B) Aspect ratio of droplets in (A) during coalescence (black). Red line is an exponential fit, with a time constant of τ = 6.33 ms. We estimate the inverse capillary velocity as $v^{-1} = \tau/d$ = 1.6 ms/μm. Error bars represent uncertainty in aspect ratio from a single coalescence event (dy) and acquisition time (dx). Conditions are 5 mM pLK, 5 mM pRE, 50 mM KCl, 1 mM $MgCl_2$, 1 mM EGTA, 10 mM imidazole (pH 7.0), and 80 μM ATP (all concentrations final).

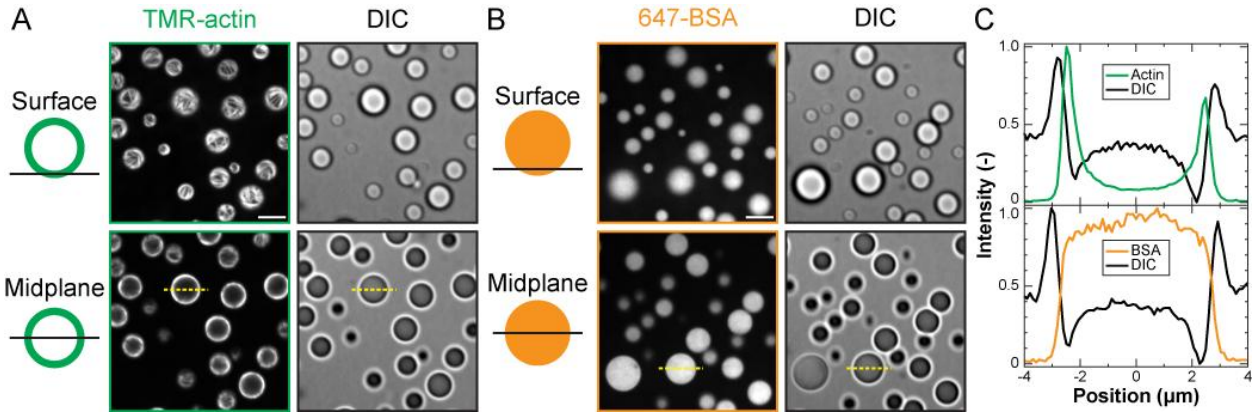

Figure S2. Peripheral localization of F-actin in polypeptide coacervates is BSA-independent. (A-B) Confocal fluorescence (left) and DIC (right) micrographs of polypeptide coacervates containing either TMR-actin (A, green) or 647-BSA (B, orange) on non-adherent substrates. Top row is focused at the interface of the coacervates and the substrate (surface), and bottom row is approximately the droplet midplane. Scale bar is 5 μm. (C) Normalized fluorescence intensity line scans along the dashed yellow lines indicated in (A) and in (B). Conditions are 0.5 μM protein (either Mg-ATP-actin (47% TMR-labeled) or BSA (91% Alexa-647-labeled)) incubated with 5 mM pLK prior to addition of 5 mM pRE in 50 mM KCl, 1 mM $MgCl_2$, 1 mM EGTA, 10 mM imidazole (pH 7.0), and 72 μM ATP (all concentrations final). Note that the average partition coefficients for (A) and (B) are reported in Figure 1 of the main text.

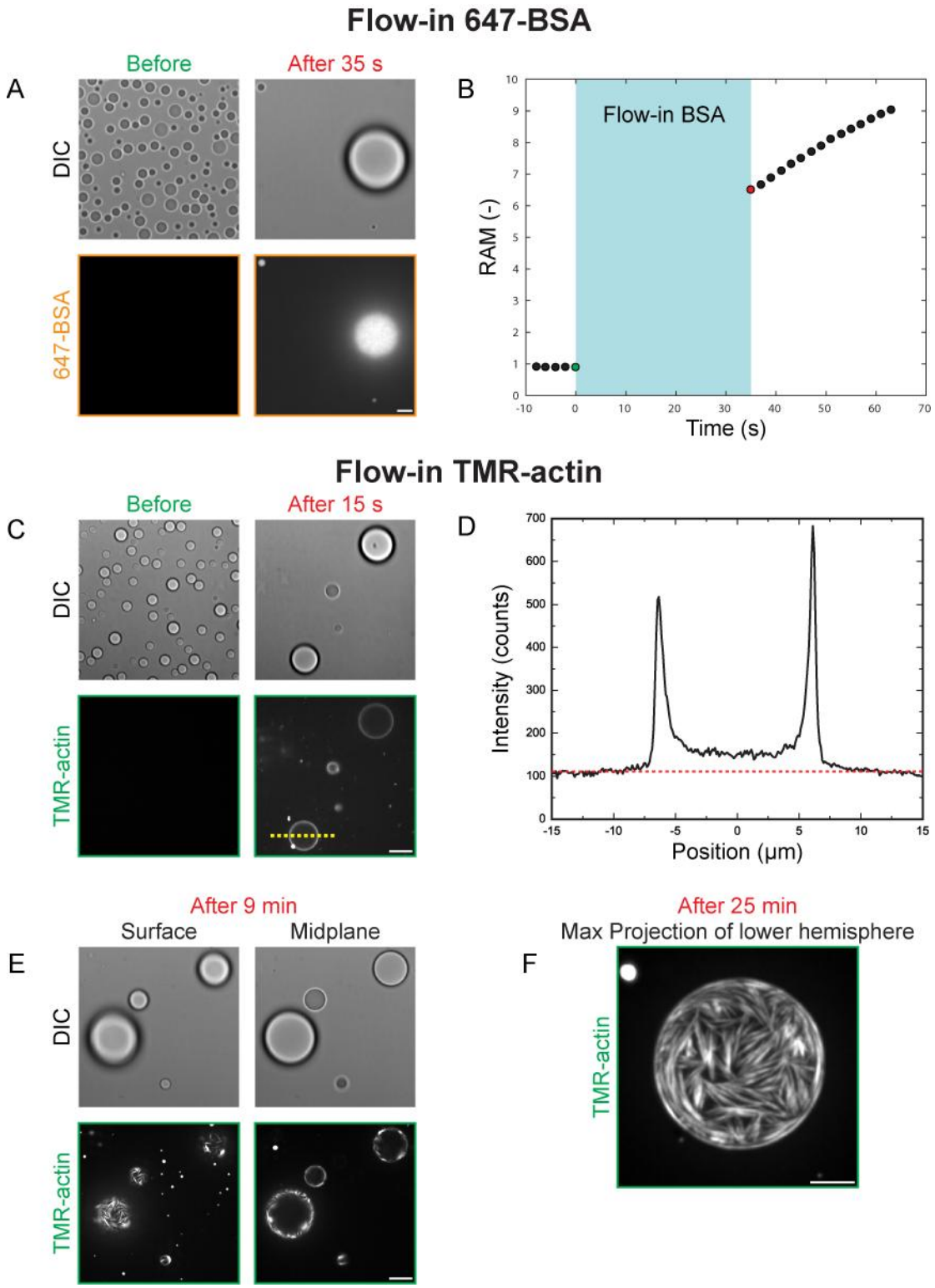

Figure S3. Flow-in of BSA or TMR-Actin to pre-formed pLK/pRE coacervates. 1.5 μM 647-BSA (A-B) or 0.25 μM TMR-actin (C-F) is perfused into a chamber containing pLK/pRE coacervates formed in the absence of protein. (A) Time-lapse confocal DIC (top) and fluorescence (bottom) micrographs of pLK/pRE coacervates before (left, green) and 35 s after (right, red) the addition of 647-BSA to the flow-cell chamber.

Figure S3. Flow-in of BSA or TMR-Actin to pre-formed pLK/pRE coacervates. (continued). Flow causes many of the sedimented droplets to fuse into larger droplets. While only background fluorescence is detectable prior to addition of BSA, BSA is partitioned to and uniformly localized within the few coacervate droplets remaining in the field of view within 35 s. Scale bar is 5 μm. (B) The RAM of the large droplet visible after BSA flow-in increases with time, but is already above 6 in the first image acquired. (C) Time-lapse confocal DIC and fluorescence micrographs before and 15 s after the addition of TMR-actin. (D) Fluorescence intensity profile along the dashed yellow line indicated in (C). The dashed red line is a guide to the eye indicating the typical fluorescence level exterior to the coacervate. Within 15 s, TMR-actin is enriched at both the periphery and interior of pLK/pRE coacervates relative to exterior levels. (E) Confocal DIC and fluorescence micrographs obtained at the coverslip surface (left) and near the coacervate midplane (right) 9 minutes following addition of TMR-actin. F-actin bundles are visible at the coacervate periphery. (F) Maximum intensity projection of confocal fluorescence micrographs obtained at 1-μm increments over an 8-μm interval. A dense network of F-actin bundles is visible. Conditions are 5 mM pLK, 5 mM pRE, 50 mM KCl, 1 mM $MgCl_2$, 1 mM EGTA, 10 mM imidazole (pH 7.0), and 72 μM ATP (all concentrations final). Proteins are perfused into the chamber in buffer containing 50 mM KCl, 1 mM $MgCl_2$, 1 mM EGTA, 10 mM imidazole (pH 7.0), and 72 μM ATP (all concentrations final). Scale bar is 5 μm in (A) and (F); 10 μm in (C) and (E).

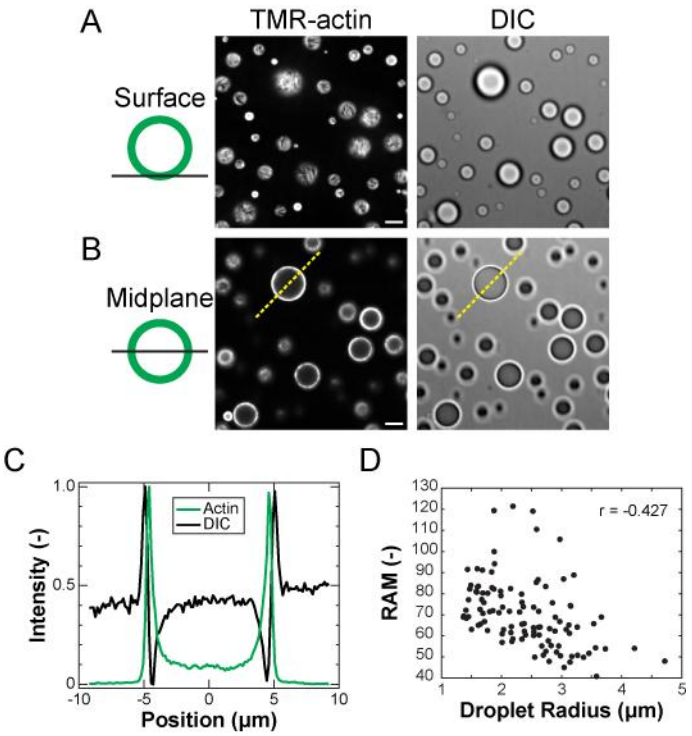

Figure S4. Partitioning and localization patterns are robust to order of addition. (A-B) Confocal fluorescence (left) and DIC (right) micrographs of polypeptide coacervates containing TMR-actin (green) on non-adherent substrates. (A) is focused at the interface of the coacervates and the substrate (surface), and (B) is approximately the droplet midplane. Scale bar is 5 μm. (C) Normalized fluorescence intensity line scans along the dashed yellow lines indicated in (B). (D) RAM of TMR-actin as a function of droplet radius, calculated for a total of N = 117 individual pLK/pRE coacervates with TMR-actin added immediately following phase separation. The average RAM is 70.3 +/- 15.9. Error bars denote the standard error of the mean. The Pearson's correlation coefficient for the data in (D) is r = -0.427, indicating a lower average partition coefficient for larger droplets. Conditions are 5 mM pLK, 5 mM pRE, 50 mM KCl, 1 mM $MgCl_2$, 1 mM EGTA, 10 mM imidazole (pH 7.0), and 72 μM ATP (all concentrations final). Following mixing and subsequent phase separation, this solution is added to a small volume of Mg-ATP-actin (47% TMR-labeled), and imaged. The final (global) concentration of actin is 0.5 μM.

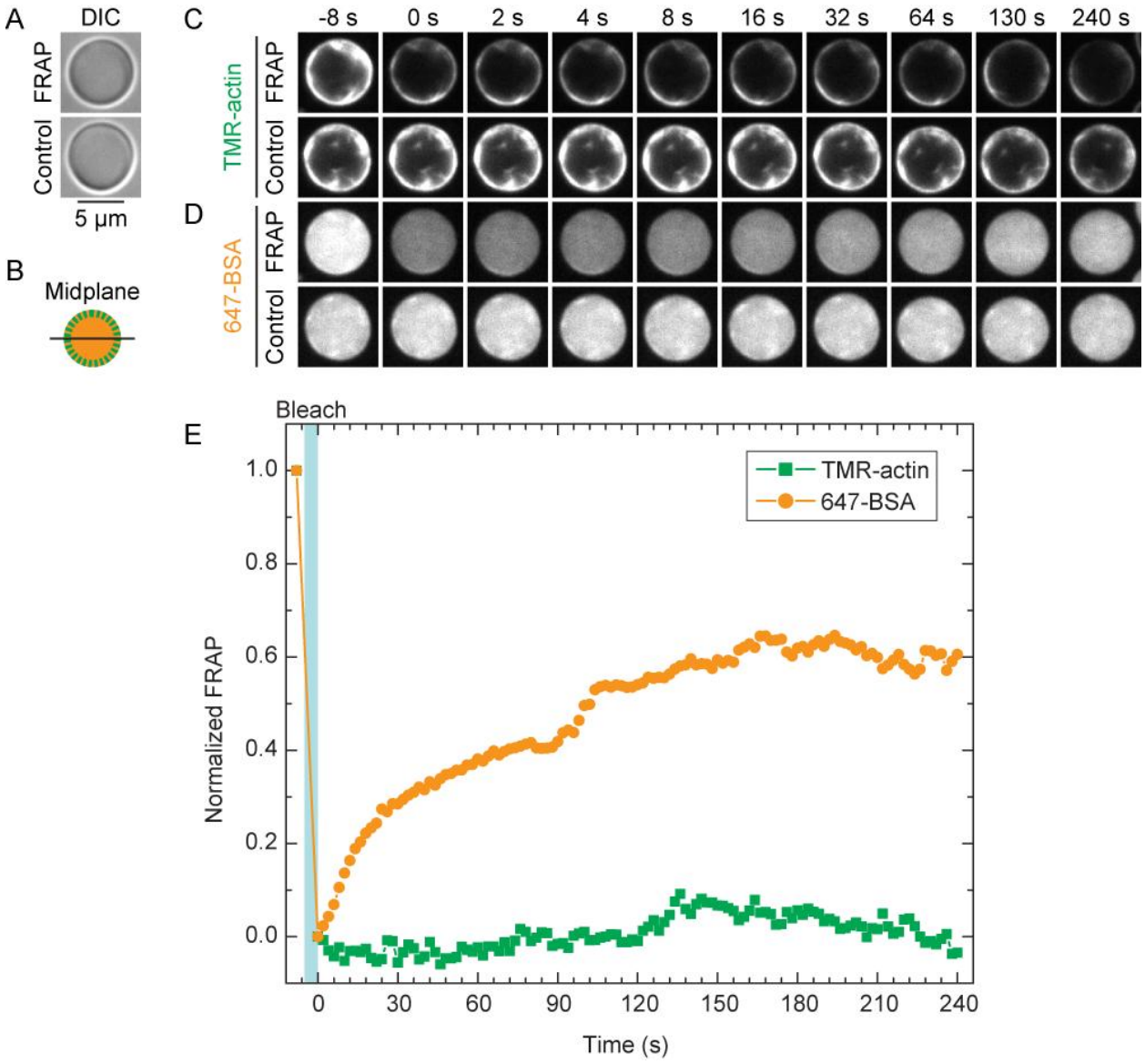

Figure S5. FRAP of partitioned actin and BSA. (A) DIC images from a single field of view of pLK/pRE coacervates into which both TMR-actin and 647-BSA are partitioned, and which are (top, FRAP) and are not (bottom, Control) subjected to a 5-second pulse of a 405-nm laser (blue shaded region in (E)). (B) Schematic denoting that images in (A) and (C-D) were acquired at the coacervate midplane. (C,D) Fluorescence images of TMR-actin (C) and 647-BSA (D) localized to coacervates which are (top rows of (C)) and (D)) and are not (bottom rows) illuminated by the bleaching laser. (E) Timecourse of the normalized average fluorescence intensity of TMR-actin (green squares) and 647-BSA (orange circles) within the coacervates shown in (C) and (D). 5-µm scale bar applies to all images. Conditions are 0.5 µM total protein (0.25 µM Mg-ATP-actin (10% TMR-labeled) and 0.25 µM BSA (91% Alexa-647-labeled)) incubated with 5 mM pLK prior to addition of 5 mM pRE in 50 mM KCl, 1 mM $MgCl_2$, 1 mM EGTA, 10 mM imidazole (pH 7.0), and 72 µM ATP (all concentrations final).

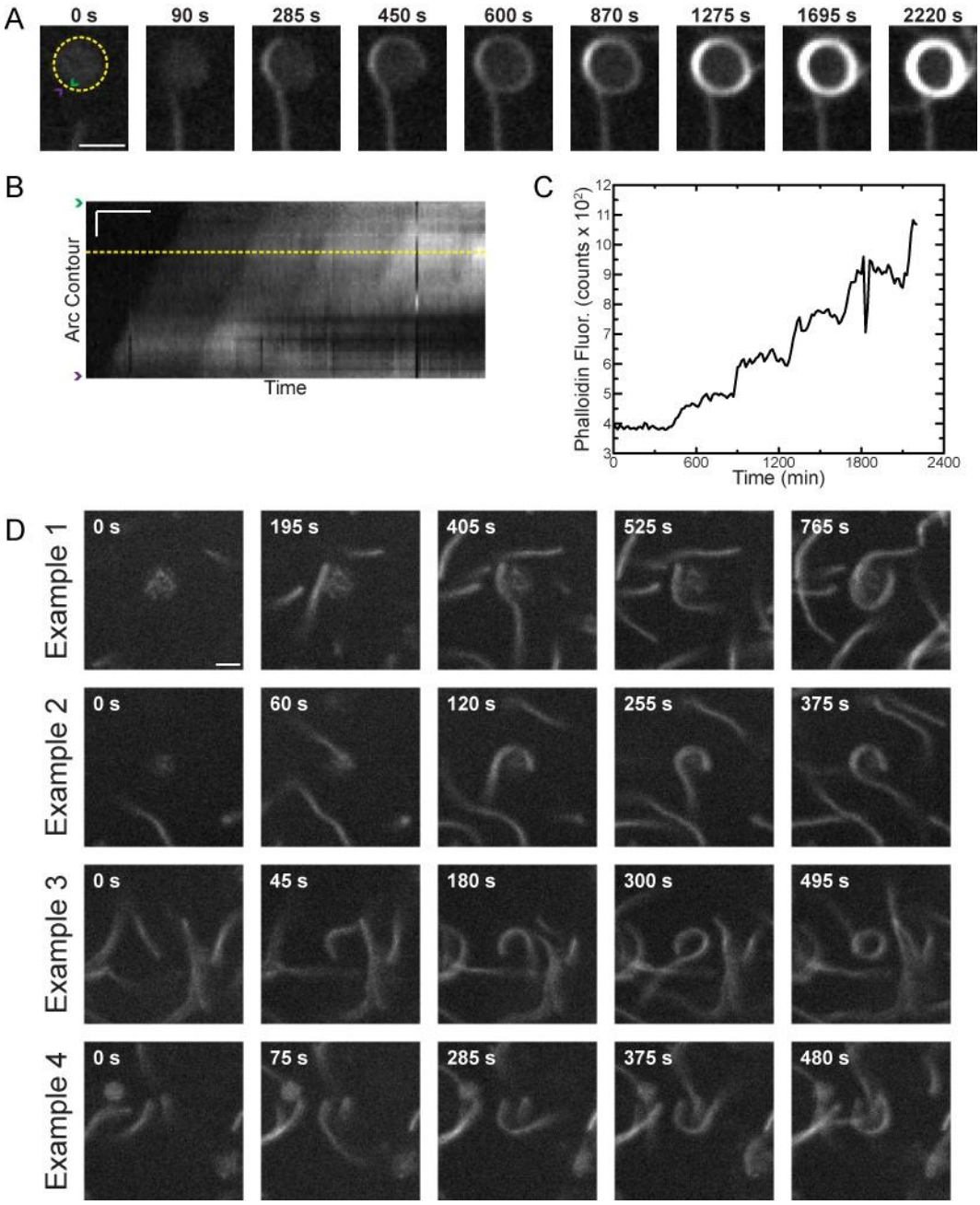

Figure S6. Adhesion of soluble F-actin to the coacervate interface. (A-D) 0.3 μM Mg-ATP-actin (unlabeled) added to a solution of 6 mM pLK/pRE coacervates and 0.2 μM Alexa488-Phalloidin in 50 mM KCl, 1 mM $MgCl_2$, 1 mM EGTA, 10 mM imidazole (pH 7.0), and 72 μM ATP (all concentrations final). (A-C) Also contain 0.5 % (w/v) 14 kDa methylcellulose (MC) and oxygen scavenging system. (A) Fluorescence time-lapse of a growing actin filament approaching a presumed coacervate droplet in presence of MC. Filament contacts coacervate, and winds around the coacervate 4 times upon further elongation. (B) Kymograph along circular yellow path in (A). (C) Intensity along yellow line scan in (B). Step-like increases indicate successive windings. (D) Examples of winding in the absence of MC. Scale bars: 2 μm (A); 1 μm and 300 s (B), 2 μm (D).

IV. SUPPLEMENTAL MOVIES

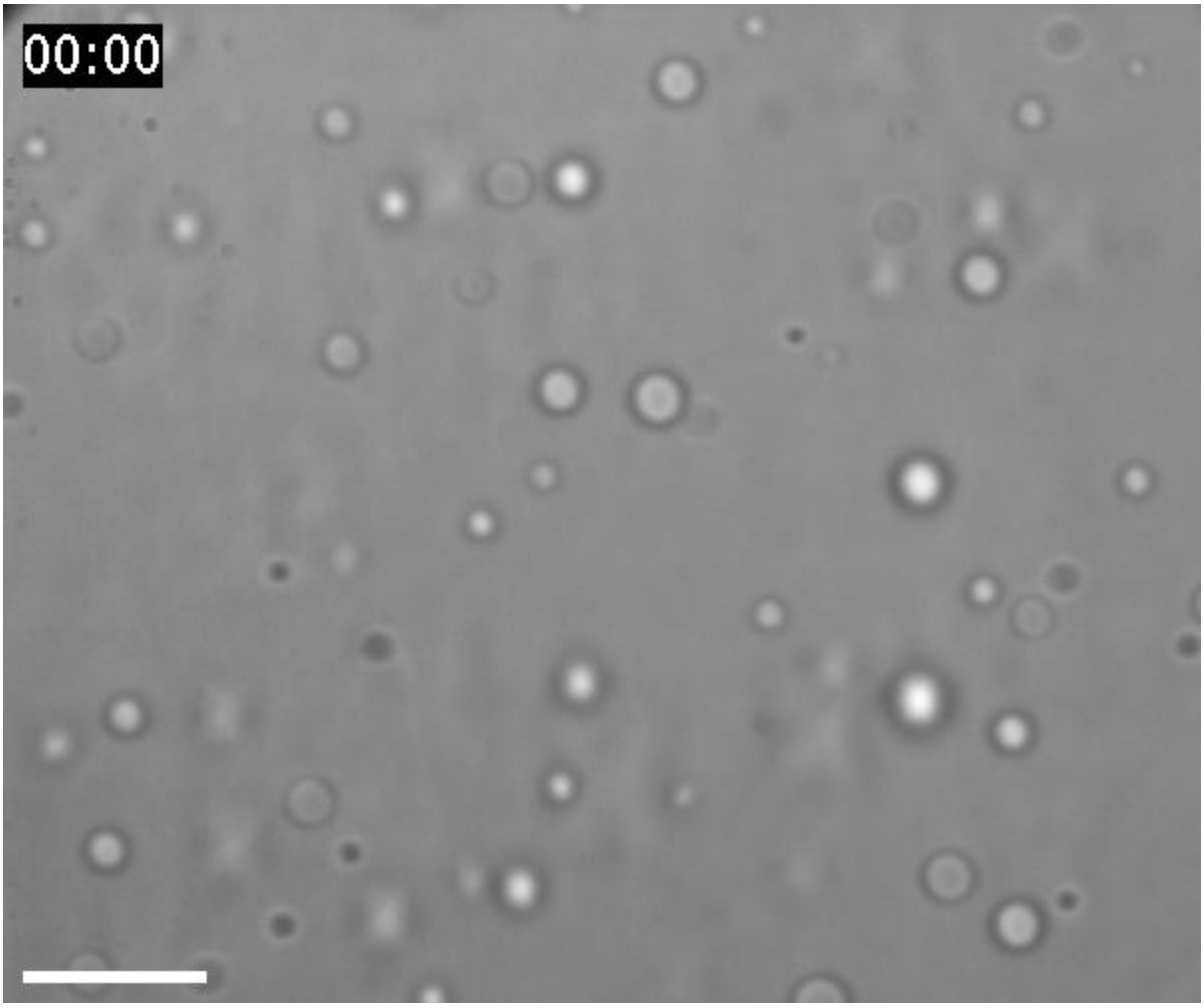

Movie S1. Coacervate droplet coalescence. Scale bar is 10 μm. Playback is 30 frames per second. Time stamp format is mm:ss. DIC timelapse imaging shows pLK/pRE coacervate droplets in solution sedimenting onto a passivated glass coverslip due to gravity. Many droplets coalescence, merging into larger droplets. Conditions are 5 mM pLK, 5 mM pRE in 50 mM KCl, 1 mM $MgCl_2$, 1 mM EGTA, 10 mM imidazole (pH 7.0), and 72 μM ATP (all concentrations final).

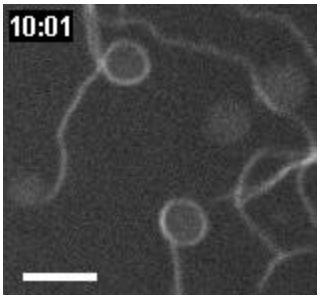

Movie S2. Adhesion of soluble F-actin to the coacervate interface. Scale bar is 4 μm. Playback is 30 frames per second. Time stamp format is mm:ss. Fluorescence time-lapse imaging shows growing actin filaments winding around presumed coacervate droplets in the presence of methylcellulose (MC). An image montage of the droplet in the lower center of the field of view is presented in Fig. S6 A. Conditions are 0.3 μM Mg-ATP-actin (unlabeled) added to a solution of 6 mM pLK/pRE coacervates and 0.2 μM Alexa488-Phalloidin in 50 mM KCl, 1 mM $MgCl_2$, 1 mM EGTA, 10 mM imidazole (pH 7.0), 72 μM ATP, 0.5 % (w/v) 14 kDa methylcellulose (MC) and an oxygen scavenging system (all concentrations final).